

On the Low-Frequency Dynamics of Turbulent Separation Bubbles

C. Cura¹, A. Hanifi², A. V. G. Cavalieri³ and J. Weiss¹

¹Institut für Luft- und Raumfahrt, Technische Universität Berlin, 10587 Berlin, Germany

²FLOW, Engineering Mechanics, KTH Royal Institute of Technology, 100 44 Stockholm, Sweden

³Divisão de Engenharia Aeronáutica, Instituto Tecnológico de Aeronáutica, 12228-900 São José dos Campos, SP, Brazil

Abstract

The low-frequency modal and non-modal stability characteristics of an incompressible, pressure-gradient-induced turbulent separation bubble (TSB) are investigated with the objective of studying the mechanism responsible for the low-frequency contraction and expansion (breathing) commonly observed in experimental studies. The configuration of interest is a TSB generated on a flat test surface by a succession of adverse and favourable pressure gradients. The base flow selected for the analysis is the average TSB from the direct numerical simulation of Coleman *et al.* (*J. Fluid Mech.*, vol. 847, 2018). Global linear stability analysis reveals that the flow is globally stable for all frequencies and wavenumbers. Furthermore, the mode closest to the stability threshold appears to occur at zero frequency and low, non-zero spanwise wavenumber when scaled with the separation length. Resolvent analysis is then employed to examine the forced dynamics of the flow. At low frequency, a region of low, non-zero spanwise wavenumber is also discernible, where the receptivity appears to be driven by the identified weakly damped global mode. The corresponding optimal energy gain is shown to have the shape of a first-order, low-pass filter with a cut-off frequency consistent with the low-frequency unsteadiness in TSBs. The results from resolvent analysis are compared to the unsteady experimental database of Le Floc'h *et al.* (*J. Fluid Mech.*, vol. 902, 2020) in a similar TSB flow. The alignment between the optimal response and the first spectral proper orthogonal decomposition mode computed from the experiments is shown to exceed 95 %, while the spanwise wavenumber of the optimal response is consistent with that of the low-frequency breathing motion captured experimentally. This indicates that the fluctuations observed experimentally at low frequency closely match the response computed from resolvent analysis. Based on these results, we propose that the forced dynamics of the flow, driven by the weakly damped global mode, serve as a plausible mechanism for the origin of the low-frequency breathing motion commonly observed in experimental studies of TSBs.

1. Introduction

Flow separation is a common phenomenon within fluid dynamics, which arises when a fluid flow is no longer able to follow the trajectory imposed by a solid wall. Such flows exhibit a variety of detrimental effects, including reduced lift, increased drag, noise emission or vibrations, all of which may negatively impact the performance of the system under consideration. A distinct subset within separated flows is the category of reattaching flows, where the flow reattaches again to the wall, e.g., due to surface

curvature or a favorable pressure gradient. This category gives rise to so-called separation bubbles, which are known to feature unsteadiness in a variety of spatial and temporal scales. In the present contribution we specifically consider turbulent separation bubbles (TSB), which occur when a turbulent boundary layer separates from the wall and reattaches further downstream. We further focus our study on pressure-gradient-induced TSBs, where detachment from a smooth surface occurs because of an adverse pressure gradient (Na & Moin 1998). This is in contrast to flows where the separation line is fixed by the surface geometry (Eaton & Johnston 1981).

Unsteadiness in pressure-induced TSBs typically occurs in three broad ranges of frequencies that may be categorized by their Strouhal number based on the separation length L_b and a reference velocity U_{ref} (Mabey 1972). For relatively high values $St > 1$, fluctuations are mainly caused by turbulent motions that have their highest amplitude in the attached flow upstream and downstream of the backflow region (Abe 2017; Le Floc’h *et al.* 2020; Wu *et al.* 2020). Within the recirculation zone, medium frequencies centered at $St \simeq 0.1 - 1.0$ appear in the wall-pressure and velocity fields due to the roll-up and shedding of vortices originating in the shear layer (Kiya & Sasaki 1983; Cherry *et al.* 1984). Finally, a low-frequency unsteadiness, typically characterized by a large-scale contraction and extension (“breathing”) of the TSB, is often observed at $St \simeq 0.01 - 0.1$ (Mohammed-Taifour & Weiss 2016). This is the main focus of the present work.

To date, low-frequency unsteadiness in pressure-induced TSBs has mostly been observed in high-speed flows, where it often occurs within shockwave/boundary layer interactions (SBLI) (Dolling 2001). There, the breathing of the TSB is associated with a low-frequency, aperiodic oscillation of a separation shock that can generate strong detrimental pressure and thermal loads on the structure, as described in the review articles by Dussauge *et al.* (2006), Clemens & Narayanaswamy (2014), and Gaitonde (2015). Recently, evidence of similar low-frequency unsteadiness has also been observed in subsonic flows. Weiss *et al.* (2015) and Mohammed-Taifour & Weiss (2016) experimentally set up a TSB on a flat test surface through the combination of an adverse and a favorable pressure gradient. They observed its low-frequency breathing at a Strouhal number similar to SBLIs ($St \simeq 0.01$). Consistent findings were also reported by Richardson *et al.* (2023) in a configuration that only featured an adverse pressure gradient (APG) but no favorable pressure gradient (FPG), by Weiss *et al.* (2022) in a turbulent half-diffuser flow, and by Dau *et al.* (2023) in the separation bubble behind a wall-mounted hump. On the numerical side, Wu *et al.* (2020) computed a configuration similar to Richardson *et al.* (2023) via direct numerical simulation (DNS) but did not capture the low frequencies observed in the experiment. On the other hand, Larchevêque (2020) showed good agreement between the characteristic frequency of the breathing motion ($St \simeq 0.01$) of flat-plate TSBs at low-subsonic, high-subsonic, and supersonic flows based on large eddy simulations (LES). This suggests that similar low-frequency behaviour occurs in a wide range of Mach numbers, as argued by Weiss *et al.* (2015, 2021).

Proposed mechanisms for the occurrence of low-frequency unsteadiness in turbulent SBLIs (and, by association, subsonic TSBs) typically consist of two main categories (Clemens & Narayanaswamy 2014): an upstream mechanism, whereby velocity fluctuations in the incoming boundary layer directly influence the position of the separation line and modulate the size of the TSB (Beresh *et al.* 2002) - in this case the low-frequency character of the unsteadiness is explained by the presence of very-large-scale turbulent structures that have been observed in both subsonic and supersonic boundary layers (Ganapathisubramani *et al.* 2003, 2007) - and a downstream mechanism, where the low-frequency unsteadiness is caused by inherent instabilities in the TSB. In the latter hypothesis, both shear layer (Piponnier *et al.* 2009) and centrifugal instabilities (Priebe

et al. 2016) have been considered. Mohammed-Taifour & Weiss (2016) discussed the relevance of these hypotheses for the case of subsonic pressure-induced TSBs but could not find any conclusive evidence to select a suitable mechanism. More recently, a third, intermediate model of low-frequency unsteadiness was put forward by Porter & Poggie (2019), who suggested that certain large-scale, near-wall perturbations in the incoming boundary layer may drive a weakly damped global mode of the separation bubble. This model inherently implies that a combination of both upstream and downstream elements is responsible for the low-frequency unsteadiness (the presence of perturbations upstream and the global mode downstream), and “reconciles the debate between upstream and downstream mechanisms of separation unsteadiness” (Porter & Poggie 2019). Such an intermediate model is also consistent with the subsonic results of Mohammed-Taifour & Weiss (2021), who experimentally demonstrated that the low-frequency behavior in their TSB is well illustrated by a first-order low-pass filter model that converts the broadband fluctuations of the incoming turbulent boundary layer into a low-frequency, large-scale oscillation of the separation and reattachment fronts.

Relevant modern frameworks for the study of low-frequency unsteadiness in separated flows are global linear stability analysis (GLSA) and resolvent analysis (RA). Both approaches rely on a linearization of the equation of motion around a suitable base flow. In the case of GLSA, the asymptotic behaviour of the homogeneous linear system is studied to reveal the presence of global modes of oscillations and their respective growth rate (Theofilis 2003, 2011). Positive growth rates suggest that inherent instabilities are present in the flow, which may then be qualified as an oscillator capable of sustaining self-excited oscillations without the presence of forcing. GLSA has broad applications to study the stability of laminar solutions (Theofilis 2011); however, when used with linearizations around the mean solution, it may provide information on dominant oscillation frequencies (Barkley 2006; Schmidt *et al.* 2017), although this cannot be ensured a priori (Sipp & Lebedev 2007). On the other hand, for globally stable flows, RA investigates the forced dynamics of the linearized flow by lumping all non-linear terms that occur in the linearization process into a forcing term (McKeon & Sharma 2010; Hwang & Cossu 2010; Cavalieri *et al.* 2019). The approach relies on the singular value decomposition (SVD) of the resolvent operator to identify the optimal forcing and its associated linear response. As such, RA may help identify specific zones of amplification in the flow, even in the absence of any global instability. When this occurs, such flows are typically characterized as amplifiers instead of oscillators (Huerre & Monkewitz 1990).

To date, most global linear analyses of separation bubbles have been conducted at relatively low Reynolds numbers, in an attempt to describe the onset of unsteadiness and three-dimensionality in laminar separated flows. Following the seminal work of Theofilis *et al.* (2000), several authors have demonstrated the existence of both oscillator- and amplifier-type dynamics in low-speed, two-dimensional laminar separation bubbles (LSB) (e.g., Marquet *et al.* 2008; Ehrenstein & Gallaire 2008; Rodríguez & Gennaro 2017). At higher Mach numbers, the topic of low-frequency unsteadiness was specifically addressed by Robinet (2007), who investigated the stability of a laminar SBLI through GLSA and demonstrated the appearance of a three-dimensional global instability when the angle of the incident shock was increased. The presence of low-frequency unsteadiness in laminar SBLIs was later confirmed by Sansica *et al.* (2016), who linked its appearance to the laminar/turbulent transition occurring in the separated shear layer and suggested that “the separation bubble acts as a low-pass spatial amplification filter”. Consistent results were recently presented by Bugeat *et al.* (2022), who related the low-frequency behaviour in a laminar SBLI to the excitation of a stable global mode. The optimal gain computed

by RA resembled a first-order low-pass filter, thereby recovering the signature of low-frequency unsteadiness typically observed in turbulent SBLIs (Poggie *et al.* 2015).

In turbulent flows, linear analyses may also be conducted by selecting the turbulent mean as base flow (Crow & Champagne 1971; Michalke 1984; Del Alamo & Jimenez 2006; McKeon & Sharma 2010; Hwang & Cossu 2010). Toubert & Sandham (2009) performed such a study on the mean flow obtained from the LES of a turbulent SBLI and found an unstable global mode that they suggested could be linked to the observed low-frequency unsteadiness. Consistent results were later obtained by Adler & Gaitonde (2018), who also discovered a global unstable mode related to low-frequency unsteadiness in a similar flow configuration. Through the use of linear stability analysis, Sasaki *et al.* (2021) suggested that upstream traveling acoustic waves are responsible for the low-frequency unsteadiness in a turbulent, incident shock interaction, thereby confirming a previous hypothesis by Pirozzoli & Grasso (2006). While all these studies proposed that turbulent SBLIs behave as oscillators, the work of Sartor *et al.* (2015) on a transonic SBLI indicated an amplifier behaviour for low-frequency perturbations. The latter conclusion was obtained by performing GLSA and RA on the average flow computed by Reynolds-Averaged Navier Stokes (RANS) simulations and comparing the results with experiments.

In this framework, the objective of the present study is to investigate the low-frequency unsteadiness of an incompressible, pressure-gradient-induced TSB by means of global stability and resolvent analysis. Specifically, we address the upstream/downstream dichotomy by examining the characteristics of global modes and their responses to external perturbations, with the aim to better understand the mechanism causing the low-frequency breathing. From a practical perspective, our motivation is three-fold: first, subsonic TSBs may serve as a reference for more complex turbulent SBLIs, where low-frequency unsteadiness is often detrimental to flight performance; second, smooth-body flow separation remains a challenge for industrial RANS turbulent modeling, which may require specific treatment for low-frequency unsteadiness; and finally, to our knowledge, such an analysis has not yet been performed in the fluid dynamics community.

The configuration that we consider is a TSB generated on a flat test surface by a combination of adverse and favourable pressure gradients. Such a flow has already been investigated experimentally by Le Floc'h *et al.* (2020) and numerically via DNS by Coleman *et al.* (2018). Our chosen methodology is to perform the linear analysis on a base flow consisting of the average DNS flow field and to validate the GLSA and RA results with the unsteady experimental database. As will be seen in the next sections, this cross-validation between two separate databases strongly supports the relevance of our findings.

The article is organised as follows. In section 2 we introduce the experimental database and demonstrate the existence of low-frequency unsteadiness from both fluctuating velocity and wall-pressure data. Then, in section 3, we describe our chosen base flow and discuss its relevance to the present investigation. The methodology for GLSA and RA is introduced in section 4 and the corresponding results are presented in section 5. These results are then compared to the experimental database and other studies in section 6 before a conclusion is offered in section 7. Specific details about the linear analysis are provided in the appendices.

2. Experimental database

In this section, we introduce the unsteady experimental database of Le Floc'h *et al.* (2018, 2020) that will be used in the present study. We briefly discuss the wind tunnel

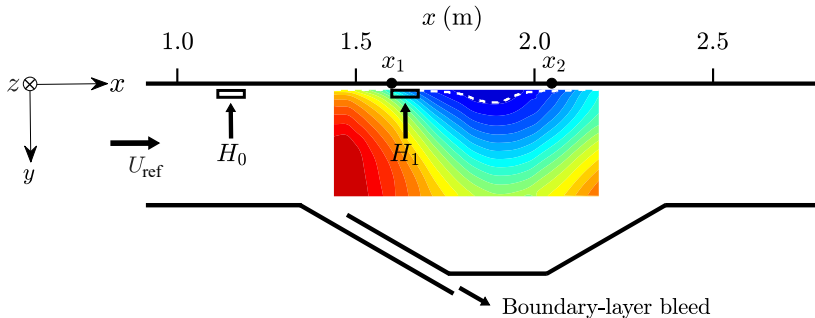


FIGURE 1. Schematic of wind tunnel test section with mean streamwise velocity field on the centerline. The time-averaged TSB is indicated by the dividing streamline $\bar{\Psi} = 0$ (- - -). H_0 and H_1 indicate the approximate position of the near-wall TR-PIV planes.

set-up, after which we proceed to outline the unsteady characteristics of the flat-plate TSB with a specific emphasis on low-frequency unsteadiness.

2.1. Experimental setup

The experiments of Le Floc’h *et al.* (2018, 2020) were conducted in the TFT boundary-layer wind tunnel, a low-speed, blow-down facility specifically designed for the study of turbulent separation bubbles (Mohammed-Taifour *et al.* 2015). The wind tunnel features a test section measuring 3 m in length and 0.6 m in width. A combination of APG and FPG is generated through the widening and subsequent converging test-section floor. Whereas the APG causes the incoming zero-pressure-gradient (ZPG) flat-plate turbulent boundary layer on the upper surface to separate, a boundary-layer bleed is located on the test-section floor to ensure that the flow on the lower surface remains attached. The FPG then forces the shear layer to reattach on the upper test surface, leading to the formation of a closed turbulent separation bubble. All experiments were performed at a reference velocity $U_{\text{ref}} = 25$ m/s and the Reynolds number of the incoming ZPG boundary layer (based on momentum thickness) was approximately 5000.

Le Floc’h *et al.* (2020) investigated TSBs of different sizes by varying the streamwise distance between the APG and FPG. Here, we primarily focus on their medium TSB, which, as will be shown in the next section, is the closest to the flow studied numerically by Coleman *et al.* (2018). The length of the medium TSB, defined as the streamwise distance between the average separation and reattachment points on the test-section centerline, is $L_b = 0.11$ m. The experimental database of Le Floc’h *et al.* (2020) includes monoscopic (two-dimensional) time-resolved Particle Image Velocimetry (TR-PIV) in the streamwise/wall-normal plane as well as unsteady wall-pressure measurements on the centerline of the test section. To illustrate the spanwise character of the low-frequency unsteadiness, these results will be complemented with unsteady wall-pressure measurements in the spanwise direction by Le Floc’h *et al.* (2018) and near-wall TR-PIV measurements in the streamwise/spanwise plane of the large TSB. The latter are unpublished data from Mohammed-Taifour & Weiss (2016).

A schematic representation of the wind-tunnel test section, with the mean streamwise velocity field measured on the centerline, is depicted in figure 1. H_0 and H_1 indicate the approximate position of the near-wall TR-PIV planes, whereas x_1 and x_2 are the streamwise positions of wall-pressure measurements (see section 2.2). While the y -axis was oriented towards the ground during the experiments, in the remainder of the article we will switch the y -direction towards the top of the page. Required descriptions of the measurement techniques will be provided in the following sections as needed. More details

on the experiments may be obtained in the original publications by Mohammed-Taifour & Weiss (2016) and Le Floc’h *et al.* (2018, 2020).

2.2. Evidence of low-frequency unsteadiness

We start by employing spectral proper orthogonal decomposition (SPOD), first introduced by Lumley (1970), to characterize the low-frequency breathing of the TSB. As opposed to the “classical” and “snapshot” POD commonly found in the recent literature, SPOD produces modes that oscillate at a single frequency (Towne *et al.* 2018). It is, therefore, a robust and powerful tool for analyzing low-frequency unsteadiness, as demonstrated for instance by the recent results of Weiss *et al.* (2022) and Richardson *et al.* (2023). In practice, we use the algorithm proposed by Towne *et al.* (2018) that is based on Welch-type averaging for stationary random processes.

In figure 2 we display the streamwise and wall-normal components \hat{u} and \hat{v} of velocity fluctuations of the leading SPOD mode, computed from the TR-PIV measurements of Le Floc’h *et al.* (2020). The PIV field-of-view is 225 mm x 75 mm ($x - y$) with a sampling frequency of $f_s = 900$ Hz. The database consists of six successive time series of $N_t = 3580$ snapshots each. Hence, the decomposition is performed on a total of $N_t = 21480$ PIV snapshots that are split in 72 blocks of $N_{\text{FFT}} = 512$ snapshots with 50% overlap. Overlapping blocks between two consecutive (uncorrelated) runs are removed. This procedure results in a frequency resolution of 1.76 Hz.

The real part of the leading mode is depicted for different Strouhal numbers $St = fL_b/U_{\text{ref}}$. A Strouhal number $St = 0.01$, typically representing the low-frequency regime, is depicted on the top (*a, b*), whereas the remaining Strouhal numbers increase from top to bottom according to $St = 0.08$ (*c, d*), $St = 0.11$ (*e, f*), and $St = 0.27$ (*g, h*). As will be discussed later (see figure 23), the first SPOD mode is particularly dominant at low frequency, with approximately 72% of the energy density at $St = 0.01$. Note that the time-averaged location of the TSB is indicated by the dividing streamline (black-dashed line) in the different plots.

In the low-frequency regime ($St = 0.01$) the streamwise component of the mode \hat{u} features a large coherent structure that bounds the TSB and follows its shape. This behavior can be observed for any low Strouhal number with $St \approx 0.01$. A similar, large-scale mode was first observed in the snapshot POD of the streamwise velocity component in Mohammed-Taifour & Weiss (2016). In their study, a low-order model was employed to show that this mode can be interpreted as a low-frequency contraction and expansion (breathing) of the TSB. More recently, SPOD has been applied to several pressure-induced TSB flows and large-scale coherent structures similar to that depicted in figure 2 (*a, b*) have been identified as the leading low-frequency SPOD mode for TSBs occurring in a one-sided diffuser (Steinfurth *et al.* 2022), behind a wall-mounted hump (Dau *et al.* 2023) and on a flat-plate with APG (Richardson *et al.* 2023). In all of these works, the aforementioned mode was associated with the low-frequency breathing of the TSB. In contrast, higher-frequency modes are qualitatively distinct: There, we observe an alternating pattern of coherent structures of opposite phase, which, in the literature, is often associated with the shedding of vortices from the shear layer bounding the recirculation region (e.g., Rajaei *et al.* 1994). The corresponding wall-normal component of the modes conveys similar trends. While in the low-frequency regime, we observe structures that encompass a significant portion of the PIV domain, an increase in the Strouhal number results in both a greater number of structures as well as smaller individual structure size.

Figure 2 (*a*) indicates that, at low frequency, the TSB contracts and expands in the streamwise direction (see also the discussion in the original article by Le Floc’h

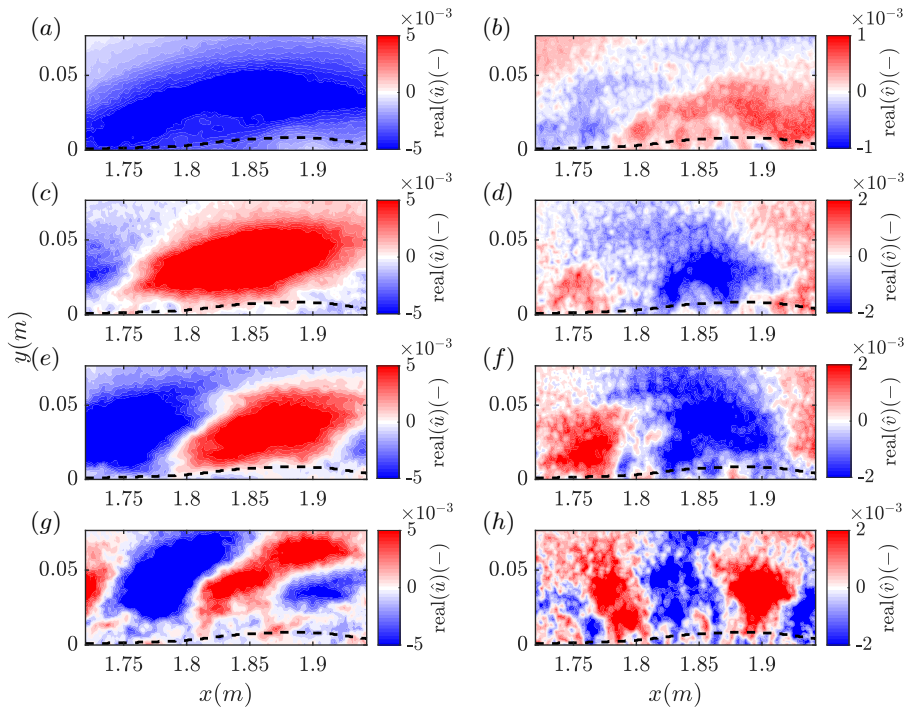


FIGURE 2. Leading SPOD mode, computed based on monoscopic PIV measurements with $f_s = 900$ Hz. The streamwise \hat{u} (a, c, e, g) and wall-normal component \hat{v} (b, d, f, h) are shown, respectively. The depicted frequencies, from top to bottom, correspond to $St = 0.01$ (a, b), 0.08 (c, d), 0.11 (e, f), 0.27 (g, h). The time-averaged location of the TSB is indicated by the dividing streamline $\bar{\Psi} = 0$ (---).

et al. 2020). In order to estimate the spanwise scale of this motion, we now consider TR-PIV measurements performed in the streamwise/spanwise plane at an elevation of $y \simeq 4$ mm away from the wall (for reference, the boundary layer thickness at position H_0 is approximately 30 mm.) These measurements were performed in the large TSB of Mohammed-Taifour & Weiss (2016) (unpublished data, see also Mohammed-Taifour (2017)). The PIV field-of-view is 75 mm x 215 mm ($x - z$) with a sampling frequency of $f_s = 900$ Hz.

The frequency-wavenumber spectra of the streamwise velocity fluctuations is depicted in figure 3. Two exemplary streamwise position are chosen, representing the spanwise ($x - z$) planes H_0 (Fig. 3 (a)) and H_1 (Fig. 3 (b)). Here, H_0 is a plane in the ZPG region upstream of the TSB and H_1 corresponds to a plane immediately upstream of the time-averaged location of the separation line, see figure 1. To extract the frequency-wavenumber spectra, we first perform a Fast Fourier Transform (FFT) in the spanwise (z) direction on $N_t = 3580$ snapshots of the fluctuating velocity u' (e.g., Towne *et al.* 2017). We further compute the power spectral density (PSD) of the Fourier-transformed signal \hat{u} adopting Welch's estimate using 50% overlap. We obtain a spectrum for each streamwise position x . Here, the frequency is represented as the Strouhal number $St = fL_b/U_{\text{ref}}$ and the non-dimensional spanwise wavenumber is $\beta = (2\pi \cdot L_b)/\lambda_z$. The chosen position corresponds to the center of each PIV measurement plane, respectively. Similar results were obtained for all investigated positions within the planes H_0 and H_1 . For visualization

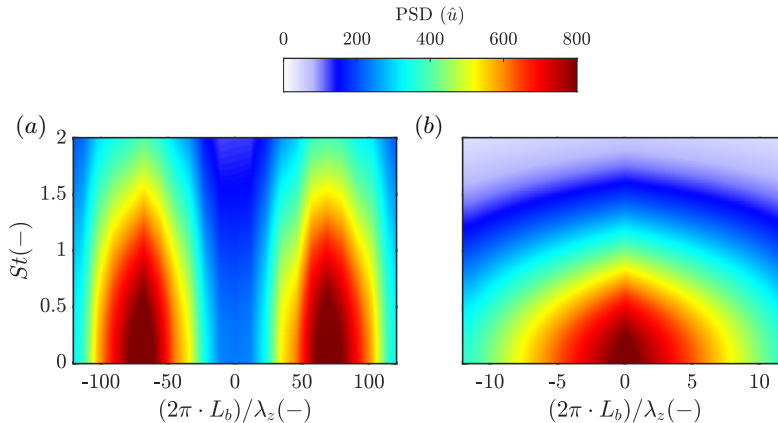


FIGURE 3. Frequency-wavenumber spectrum of fluctuating velocity u' in the $x - z$ plane at $y \simeq 4$ mm from the test surface. Two streamwise positions x are depicted, a position in the ZPG region upstream of the TSB $x = 1.33$ m (a) and a position immediately upstream of the time-averaged location of the separation line $x = 1.68$ m (b). The spanwise wavenumber $\beta = 2\pi/\lambda_z$ is non-dimensionalized by the average bubble length L_b . The PSD in the ZPG region (a) is multiplied by a factor of 10.

purposes, the PSD of \hat{u} is scaled by a factor of 10 for the H_0 plane in the upstream boundary layer (Fig. 3 (a)).

In the upstream ZPG boundary layer (H_0 plane), the maximum of the PSD of \hat{u} is obtained for the non-dimensional spanwise wavenumber $\beta = \pm 65$ and a Strouhal number range of $St \leq 0.8$ (Fig. 3 (a)). All frequencies St in the vicinity of $\beta = \pm 65$ exhibit fairly high energy levels. However, no substantial energy content can be detected in the region of two-dimensional perturbations $\beta = 0$. Moreover, since the spectrum is symmetrical with respect to $\beta = 0$, no preferential z -direction can be detected for the present configuration. This indicates that perturbations are equally likely to propagate in the $+z$ and $-z$ direction. When expressed in terms of the boundary layer thickness $\delta = 28$ mm of the incoming turbulent flow (measured at $x = 1.1$ m), the spanwise wavelength λ_z , related to the non-dimensional spanwise wavenumber $\beta = \pm 65$, is approximately $\lambda_z = 0.4\delta$. This value is in agreement with the values of $\mathcal{O}(\delta)$ reported for the superstructures in the upstream boundary layer of several turbulent boundary layer flows (e.g., Tomkins & Adrian 2003; Hutchins & Marusic 2007; Le Floch *et al.* 2016). Interestingly, a similar organization of elongated structures over the span of the H_0 measurement plane can also be observed on the first SPOD modes at low frequency (not shown here).

In figure 3 (b) we display the representative frequency-wavenumber spectrum of the measurement-plane H_1 . The majority of the energetic content is now gathered in the range $-2 \leq \beta \leq 2$. Once again, the distribution is symmetrical with respect to $\beta = 0$, indicating no preferential z -direction. On the other hand, the wavelengths λ_z associated with the structures of this low- β range are now large compared to the bubble length L_b . They take values between $\lambda_z = 3L_b$ for $\beta = \pm 2$ to $\lambda_z \gg 10L_b$ for very small β . Hence, the low-frequency unsteadiness of the TSB appears to be coherent over a large spanwise scale. Furthermore, the high- β signature observed in the incoming ZPG boundary layer is absent from the frequency-wavenumber spectrum close to the separation line, thereby suggesting that the TSB is not directly responding to the long superstructures present in the incoming boundary layer.

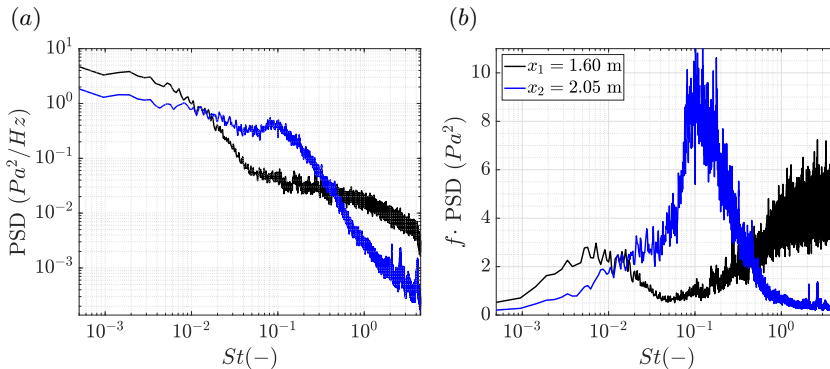


FIGURE 4. Power spectral density (PSD) (a) and pre-multiplied PSD (b) of fluctuation pressure p' for $x_1 = 1.60$ m (black) and $x_2 = 2.05$ m (blue). The Strouhal number St is calculated based on the bubble length L_b and the reference velocity $U_{\text{ref}} = 25 \text{ m s}^{-1}$.

To confirm these results, we now consider fluctuating wall-pressure data gathered in the spanwise direction by Le Floc'h *et al.* (2018) in the medium TSB again. All pressure signals were obtained by using piezoresistive pressure transducers with a range of 1 psi (6.89 kPa) and an estimated error of $\pm 5\%$. To eliminate low-frequency wind-tunnel noise in the signals, the correction method from Weiss *et al.* (2015) was applied. PSDs were calculated by adopting Welch's method using 50% overlap and a Hamming window.

In figure 4, the classical log-log PSD (a) and the pre-multiplied PSD (b) of the fluctuating wall pressure p' on the test-section centerline at two streamwise positions are shown: a position immediately upstream of the time-averaged location of the separation bubble ($x_1 = 1.60$ m) and a position in the region downstream of the TSB ($x_2 = 2.05$ m). These streamwise positions are depicted schematically in figure 1. The low-frequency unsteadiness becomes apparent as a distinct ‘‘hump’’ in the pre-multiplied distribution for $x_1 = 1.60$ m, where a significant amount of energy is gathered in the region $St \approx 0.01$. This hump has also been observed by Mohammed-Taifour & Weiss (2016) and Richardson *et al.* (2023), and has been associated to the low-frequency breathing of their TSB. On the other hand, a different behavior can be observed for $x_2 = 2.05$ m. Here, a distinct peak is visible in the pre-multiplied PSD for $St \approx 0.1$. In Cura *et al.* (2023), this medium-frequency unsteadiness was linked to instabilities in the shear layer bounding the recirculation region.

Coming back to the spanwise characteristics of low-frequency unsteadiness, we show in figure 5 (a) the two-point cross-correlation coefficient at zero time lag measured by Le Floc'h *et al.* (2018). Here, $R_{p'p'} = \overline{p'(z) * p'_{\text{ref}}(z_{\text{ref}})} / (p'_{\text{rms}} * p'_{\text{ref,rms}})$ was obtained by simultaneously measuring the wall-pressure fluctuations at the centerline of the test section ($z_{\text{ref}} = 0$ mm) and with a moving sensor positioned successively at $z = [0, \pm 0.05, \pm 0.10, \pm 0.15, \pm 0.20]$ m along the span of the wind-tunnel test section. Furthermore, all pressure signals were low-pass filtered to frequencies below $St = 0.03$ before computing the cross-correlations, so that only values that correspond to the low-frequency hump in figure 4 are considered. Again, two streamwise positions, $x_1 = 1.60$ m and $x_2 = 2.05$ m, are depicted. In both cases, a wave-like distribution of $R_{p'p'}$ over the span, with a relatively large wavelength λ_z , becomes apparent. This confirms that the low-frequency unsteadiness is coherent over a large portion of the test-section span.

To obtain a quantitative metric of spanwise coherence, we now perform a curve-fit of

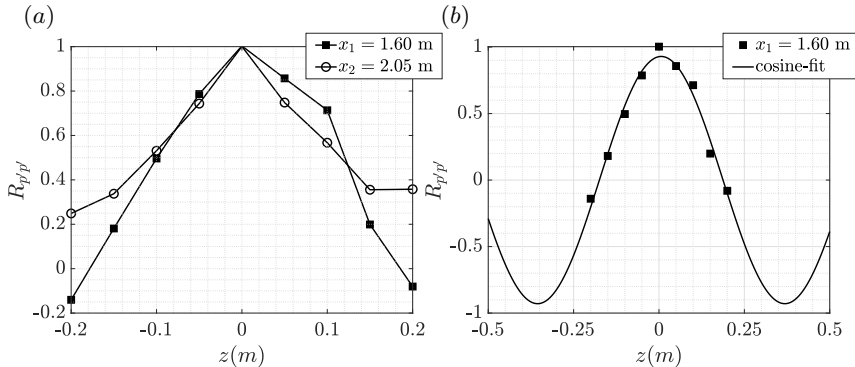


FIGURE 5. Spanwise correlation $R_{p'p'}$ of low-pass filtered fluctuating pressure for two streamwise positions $x_1 = 1.60$ m (\blacksquare), $x_2 = 2.05$ m (\circ) modified from Le Floc'h *et al.* (2018) (a) and cosine-fit $f(z) = c_1 \cdot \cos(c_2 z)$ of $R_{p'p'}$ (---) at $x_1 = 1.60$ m (b). The resulting non-dimensional spanwise wavenumber $\beta = (2\pi \cdot L_b)/\lambda_z$ is equal to 0.97. The fluctuating pressure at the test-section centerline ($z = 0$ m) is used as reference for all correlations.

the correlation curve at $x_1 = 1.60$ m, using a cosine function of the form

$$f(z) = c_1 \cdot \cos(c_2 z). \quad (2.1)$$

We obtain the distribution shown in figure 5 (b), where the cosine-function has a non-dimensional spanwise wavenumber $\beta = 0.97$. This value is in the energy-containing range observed in the frequency-wavenumber spectrum of near-wall velocity data in figure 3 (b). Notably, this results closely matches the spanwise wavenumber corresponding to the width of the wind tunnel $b = 0.6$ m, which is $\beta = 1.17$.

In summary, the experimental results obtained by Le Floc'h *et al.* (2018, 2020), using both fluctuating velocity and wall-pressure measurements, indicate that the TSB is contracting and expanding at low frequency, with a characteristic Strouhal number of the order of $St = fL_b/U_{\text{ref}} = 0.01$. This breathing motion appears to be reasonably coherent across the span, with a spanwise wavenumber of the order of $\beta = (2\pi \cdot L_b)/\lambda_z = 1$. In the remainder of the article, our main objective will be to use global linear stability and resolvent analysis to try and explain the origin of this motion.

3. Numerical database

In this work, we perform modal and non-modal stability analysis of the time- and spanwise averaged velocity field from the DNS by Coleman *et al.* (2018). Our motivation in doing so is mainly that employing an experimental flow field as base flow for stability analysis would typically require some degree of curve-fitting and/or extrapolation (e.g. Nishioka *et al.* (1990); Yarusevych *et al.* (2006)). This is mostly due to the inherent characteristics of experimental velocity fields, which typically exhibit considerable data scatter. Both the application of curve-fitting techniques and the presence of data scatter are well-documented phenomena known to significantly influence the outcomes of local linear stability analysis (e.g., Dovgal *et al.* 1994; Bottaro *et al.* 2003; Boutilier & Yarusevych 2013). Furthermore, velocity fields measured by TR-PIV typically suffer from poor spatial resolution because of the relatively large pixel size of CMOS cameras (Le Floc'h *et al.* 2020). On the contrary, a DNS base flow usually provides a higher spatial

resolution and a larger domain size than its experimental counterpart, hence facilitating the computation of the required derivatives in the stability analysis.

A typical GLSA/RA study on a DNS base flow would usually be compared to unsteady DNS data. Here, we do not follow this path but we compare our results to the experimental database of Le Floc’h *et al.* (2018, 2020) summarized in the last section. Our motivation for doing so is two-fold. First, Coleman *et al.* (2018) could not observe any low-frequency breathing motion in their DNS data because of limited computing resources. Indeed, capturing low-frequency unsteadiness requires very long integration times that are still difficult to reach for well-resolved simulations. Similarly, Wu *et al.* (2020) were not able to capture $St \simeq 0.01$ -phenomena in their own DNS. Hence, to the authors’ knowledge, the low-frequency unsteadiness has not been observed in any simulation of low-speed TSB yet. Our second motivation is that, if the linear analysis on the DNS base flow favorably compares to the experimental results, it would strongly support the generality and portability of our results, and also rule out that the breathing is caused by an experimental artifact. Therefore, although the DNS of Coleman *et al.* (2018) was not originally designed to match our experimental TSB flow, we contend that the merits of our strategy outweigh its drawbacks.

The flow field of Coleman *et al.* (2018) was selected because of its similarity to the experimental set-up and its free accessibility (Coleman 2018). The DNS features a fully turbulent, two-dimensional flat-plate boundary layer, which is subjected to an APG subsequently followed by an FPG. The APG-FPG characteristics are enforced by a transpiration velocity profile $V_{\text{top}}(x)$, introduced on a virtual parallel plane at a fixed distance opposite to the no-slip wall (Eq. 3.1). Here, V_{max} is the maximum velocity of the transpiration velocity profile and ξ is the length scale. To enforce the ZPG along the wall, a constant boundary-layer bleed velocity ϕ_{top} is introduced. A pseudo-spectral code was used to compute the solution to the incompressible Navier-Stokes equations. Further details regarding the DNS can be found in Coleman *et al.* (2018). In the following, only the mean flow field from case C (main case) will be considered.

$$V_{\text{top}}(x) = -\sqrt{2}V_{\text{max}}\left(\frac{x}{\xi}\right)\exp\left(\frac{1}{2} - \left(\frac{x}{\xi}\right)^2\right) + \phi_{\text{top}} \quad (3.1)$$

The similarities between the DNS (Case C) and the experimental (medium) TSB were already outlined in Le Floc’h *et al.* (2020). Here, we demonstrate that the two TSB flows exhibit an even higher degree of similarity when an appropriate set of scaling parameters is selected. For this purpose, we introduce the parameter L_p , which is equal to the distance between the maximum APG and FPG. We further introduce the momentum thickness Θ_0 , which was computed by means of the von Kármán integral $d\Theta/dx = c_f/2$. It correspond to the momentum thickness that would be reached at the streamwise position $x(V_{\text{top}} = 0)$ for a ZPG boundary layer (Coleman *et al.* 2018).

In figure 6 we plot the streamwise velocity u/u_∞ of the experimental flow from Le Floc’h *et al.* (2020) (a) and the DNS calculations from Coleman *et al.* (2018) (b). The streamwise and wall-normal coordinates are non-dimensionalized by the distance L_p and the momentum thickness Θ_0 , respectively. For each flow, we indicate the time-averaged location of the TSB by means of the $\bar{u} = 0$ contourline (white-solid line) and the dividing streamline (white-dashed line). In this scaling, the flow databases become very similar, with a comparable position of mean flow separation and reattachment. In figure 6 (c), the pressure distribution along the flat plate, as indicated by the pressure coefficient c_p , is displayed. The solid line represents the DNS, whereas symbols pertain to the wall-pressure measurements. In contrast to the contour plots of streamwise velocity u/u_∞ , some discrepancies between the DNS base flow and the experimental data become

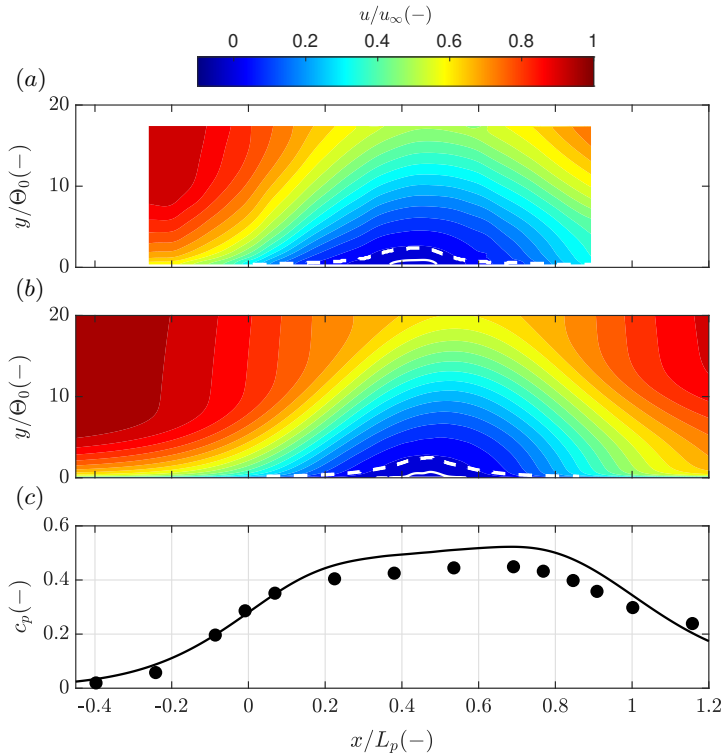


FIGURE 6. Streamwise velocity component u/u_∞ of experimental flow field (a) and DNS base flow (b). The pressure distribution along the flat plate is represented by the pressure coefficient c_p (c) for the DNS base flow (—) and the experimental data (\bullet). The streamwise and wall-normal coordinates are non-dimensionalized by L_p and Θ_0 , respectively. We indicate the time-averaged position of the TSB by the $\bar{u} = 0$ contourline (—) and the dividing streamline (---).

Database	$Re_{\Theta_0}(-)$	$Re_{L_b}(-)$	$L_b/\Theta_0(-)$	$L_p/\Theta_0(-)$
Medium TSB (Le Floc'h <i>et al.</i> (2020))	6905	183673	26.6	154.5
Case C (Coleman <i>et al.</i> (2018))	3121	104000	33.3	207.5

TABLE 1. Flow characteristics of experimental and numerical database.

evident. The plateau in the distribution of c_p is reached for a higher value in the case of the DNS. However, up to $x/L_p \approx 0.9$, the distributions remain in good qualitative agreement. While acknowledging the non-identical nature of both flows, we operate under the assumption that insights derived from the linear analysis of the DNS base flow can be transferred to the experimental counterpart. This assumption will be re-evaluated in the discussion section of this paper. The key characteristics of each flow database are summarized in table 3.

4. Methodology

In this section, the governing equations describing the dynamics of the turbulent separation bubble (TSB), as well as the employed stability and data analysis methods, are described.

4.1. Governing equations

The viscous incompressible Navier-Stokes equations for the conservative variables $\mathbf{q} = (u, v, w, p)$

$$\nabla \cdot \mathbf{u} = 0, \quad \frac{\partial \mathbf{u}}{\partial t} + \mathbf{u} \cdot \nabla \mathbf{u} = -\nabla p + \frac{1}{Re} \nabla^2 \mathbf{u}, \quad (4.1)$$

are considered, where $\mathbf{u} = (u, v, w)$ are the streamwise, wall-normal and spanwise velocity, respectively, p is the pressure, and Re is the Reynolds number. Here, we decompose the flow field into time-averaged and fluctuating quantities according to

$$\mathbf{q}(x, y, z, t) = \bar{\mathbf{q}}(x, y, z) + \tilde{\mathbf{q}}(x, y, z, t). \quad (4.2)$$

Introducing the above Reynolds decomposition (Eq. 4.2) into the incompressible Navier-Stokes equations (4.1) and time-averaging yields the linearized Navier-Stokes equations (LNSE)

$$\frac{\partial \tilde{\mathbf{u}}}{\partial t} + \tilde{\mathbf{u}} \cdot \nabla \bar{\mathbf{u}} + \bar{\mathbf{u}} \cdot \nabla \tilde{\mathbf{u}} = -\nabla \tilde{p} + \frac{1}{Re} \nabla^2 \tilde{\mathbf{u}} + \tilde{\mathbf{f}}, \quad (4.3)$$

$$\nabla \cdot \tilde{\mathbf{u}} = 0. \quad (4.4)$$

Here, we group the non-linear terms in the Navier-Stokes equations into a forcing term $\tilde{\mathbf{f}}$, as proposed by McKeon & Sharma (2010). In the work of Towne *et al.* (2018) it was demonstrated that when the forcing term is modelled as spatial white noise, a direct relationship between SPOD and resolvent modes can be expected. However, turbulent flows have non-linear terms that differ from such white-noise approximation, and thus have colour (Zare *et al.* 2017; Morra *et al.* 2021; Nogueira *et al.* 2021). When linearizing around a turbulent mean flow, the colour of the forcing is often partly incorporated by means of an eddy-viscosity model (Morra *et al.* 2019, 2021). Here, we follow the methodology outlined in Reynolds & Hussain (1972) and represent part of the Reynolds stresses by means of an eddy-viscosity model

$$\frac{\partial \tilde{\mathbf{u}}}{\partial t} + \tilde{\mathbf{u}} \cdot \nabla \bar{\mathbf{u}} + \bar{\mathbf{u}} \cdot \nabla \tilde{\mathbf{u}} = -\nabla \tilde{p} + \frac{1}{Re} (1 + \nu_t/\nu) \nabla^2 \tilde{\mathbf{u}} + \tilde{\mathbf{f}}. \quad (4.5)$$

The eddy viscosity is calculated from the DNS data provided in Coleman *et al.* (2018) as $\nu_t = c_\mu k^2/\varepsilon$ (see Fig. 7). Here $c_\mu = 0.09$, k is the turbulent kinetic energy, and ε is the dissipation rate.

4.2. Global linear stability analysis

When the forcing term is set to $\tilde{\mathbf{f}} = 0$, the system of equations (4.3-4.4) can be recast in matrix form as

$$\mathbf{M} \frac{\partial \tilde{\mathbf{q}}}{\partial t} = \mathbf{A}_{3D} \tilde{\mathbf{q}}, \quad (4.6)$$

where \mathbf{A}_{3D} is the three-dimensional LNSE operator. Choosing a modal ansatz of the form

$$\tilde{\mathbf{q}}(x, y, z, t) = \hat{\mathbf{q}}(x, y, z) \exp(-i\omega t) + c.c., \quad (4.7)$$

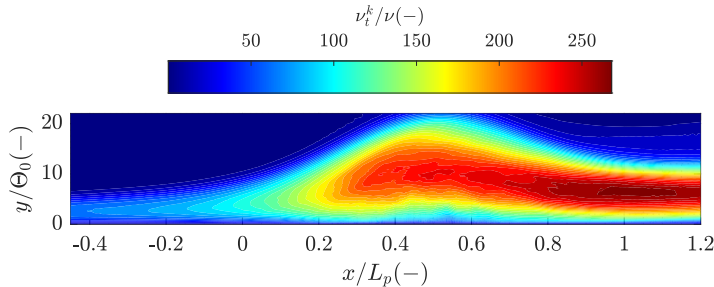


FIGURE 7. Eddy viscosity calculated from DNS data.

and introducing it into the LNSE (4.3-4.4) leads to a generalized eigenvalue problem (EVP)

$$-i\omega\mathbf{M}\hat{\mathbf{q}}(x, y, z) = \mathbf{A}_{3D}(\bar{\mathbf{q}}(x, y, z), Re)\hat{\mathbf{q}}(x, y, z), \quad (4.8)$$

where c.c. is the complex conjugate, $\omega \in \mathbf{C}$ are the eigenvalues, and $\hat{\mathbf{q}}$ are the eigenfunctions. We now assume homogeneity in the spanwise direction z and perform a Fourier transform in space, such that equation (4.7) reduces to

$$\tilde{\mathbf{q}}(x, y, z, t) = \hat{\mathbf{q}}(x, y)\exp[i(\beta z - \omega t)] + c.c., \quad (4.9)$$

and the EVP can be reformulated as

$$-i\omega\mathbf{M}\hat{\mathbf{q}}(x, y) = \mathbf{A}_{2D,z}(\bar{\mathbf{q}}(x, y), \beta, Re)\hat{\mathbf{q}}(x, y). \quad (4.10)$$

Here, $\beta \in \mathbf{R}$ is the spanwise wavenumber. The two-dimensional LNSE operator $\mathbf{A}_{2D,z}$ can be extracted from \mathbf{A}_{3D} by introducing $\bar{\mathbf{u}} = (\bar{u}, \bar{v}, 0)$ and employing equation (4.9). The operator can then be divided into $\mathbf{A}_{2D,z} = \mathbf{A} + \mathbf{N}$, where \mathbf{N} represents the (additional) turbulence terms modeled in equation (4.5). The EVP in equation (4.10) needs to be supplemented with appropriate homogeneous boundary conditions to fulfill the physical constraints on the domain (see Appendix B). The spanwise-periodic EVP can then be analyzed to yield unstable global modes whenever the growth rate $\omega_i > 0$, whereas disturbances decay in the asymptotic time limit for $\omega_i < 0$.

The LNSE operator $\mathbf{A}_{2D,z}$ and operator \mathbf{M} are included in Appendix A. The solution of the 2D EVP is performed using the code presented in Abreu *et al.* (2021) and Blanco *et al.* (2022), adapted for global stability analysis. A grid and fringe convergence study was performed and is summarized in Appendix C. All quantities appearing in the linear analysis are non-dimensionalized by means of the length scale $l^* = L_b$ and the time-scale $t^* = L_b/u_\infty$. The resulting Reynolds number based on u_∞ and L_b is $Re = 104000$. On the other hand, in order to plot the results in a manner consistent with the experiments, the streamwise and wall-normal coordinates of the TSB are represented as x/L_p and y/Θ_0 , respectively.

4.3. Resolvent analysis

In order to study the linear forced dynamics of the system, we now consider equation (4.10) and re-introduce the forcing term on the right-hand-side

$$-i\omega\mathbf{M}\hat{\mathbf{q}} = \mathbf{A}_{2D,z}\hat{\mathbf{q}} + \mathbf{B}\hat{\mathbf{f}}, \quad (4.11)$$

where the harmonic forcing is $\hat{\mathbf{f}} = (f_x, f_y, f_z, 0)$. This system can be rewritten in the resolvent form

$$(-i\omega\mathbf{M} - \mathbf{A}_{2D,z})\hat{\mathbf{q}} = \mathbf{B}\hat{\mathbf{f}}. \quad (4.12)$$

The optimal response $\hat{\mathbf{q}}$ to any harmonic forcing $\hat{\mathbf{f}}$ can be obtained by performing a singular value decomposition (SVD) of the resolvent operator \mathbf{R}

$$\hat{\mathbf{q}} = \mathbf{C}(-i\omega\mathbf{M} - \mathbf{A}_{2D,z})^{-1}\mathbf{B}\hat{\mathbf{f}} = \mathbf{R}\hat{\mathbf{f}}, \quad (4.13)$$

where the operators \mathbf{B} and \mathbf{C} act as filters that impose restrictions on the forcing (input) and the response (output), respectively. The first singular value of the SVD of the resolvent operator is then the optimal gain σ_1 , whereas the left and right singular vectors represent the optimal forcing and response, respectively. The remaining singular values of the SVD are called the sub-optimal gains, and are arranged in decreasing order $\sigma_1 > \sigma_2 > \sigma_3 > \dots > \sigma_n$. The solution to the SVD in equation (4.13) is computed using the code presented in Abreu *et al.* (2021) and Blanco *et al.* (2022). The operators \mathbf{B} and \mathbf{C} are discussed in more detail in Appendix A. The study conducted by Towne *et al.* (2018) demonstrated a direct relationship between the optimal response obtained from RA and the modes extracted from SPOD, under the assumption that the forcing is modeled as spatial white noise. Even though non-linearities in the Navier-Stokes equations are expected to have ‘‘colour’’ (Zare *et al.* 2017), a strong link between RA and SPOD can be expected if the CSD is dominated by the optimal response (Cavaliere *et al.* 2019). This is the case when the leading resolvent mode is of low-rank, such that $\sigma_1 \gg \sigma_2$.

In order to quantify the alignment between SPOD and RA (Lesshafft *et al.* 2019; Abreu *et al.* 2020) for several spanwise wavenumbers β , we introduce the metric

$$\varphi = \frac{\langle \hat{q}_{1\text{SPOD}}, \hat{q}_{1\text{RA}} \rangle}{\|\hat{q}_{1\text{SPOD}}\| \cdot \|\hat{q}_{1\text{RA}}\|}, \quad (4.14)$$

which consists of the projection of the first SPOD mode $\hat{q}_{1\text{SPOD}} = [\hat{u}_{1\text{SPOD}}, \hat{v}_{1\text{SPOD}}]$ on the first resolvent mode $\hat{q}_{1\text{RA}} = [\hat{u}_{1\text{RA}}, \hat{v}_{1\text{RA}}]$. Here \hat{u}_1, \hat{v}_1 are the streamwise and wall-normal components of the first SPOD and first resolvent mode, respectively. Furthermore, $\langle \cdot, \cdot \rangle$ is the L_2 inner product and $\|\cdot\|$ is the euclidean norm. The value $\varphi = 1$ corresponds to perfect alignment of the modes, whereas $\varphi = 0$ indicates that the modes are orthogonal. Note that only the streamwise and wall-normal component are considered here, as the high-speed PIV data was taken in a monoscopic arrangement for which no information on the spanwise velocity component is available (Le Floc’h *et al.* 2020).

5. Results

5.1. Global stability analysis

We initiate the analysis by investigating the spectral characteristics of the base flow, as well as the influence of the non-dimensional spanwise wavenumber on the GLSA spectrum. Figure 8 illustrates the growth rate of the eigenvalues for the two-dimensional ($\beta = 0$) and the three-dimensional case ($\beta = 0.75$). Growth rates ω_i and Strouhal numbers $St = f \cdot L_b / u_\infty$ are depicted. The stability threshold is shown as a grey shaded region. As can be seen, all growth rates ω_i are negative, indicating that all modes are globally stable. Moreover, the GLSA spectra display similar shapes, where the least stable mode of each spectrum (2D/3D) is a ‘‘stationary’’ mode ($St = 0$) and the subsequent modes (2 – 4) are ‘‘travelling’’ modes ($St \neq 0$). The stationary nature of the least stable mode of the GLSA is in good agreement with the modal analyses of Theofilis *et al.* (2000),

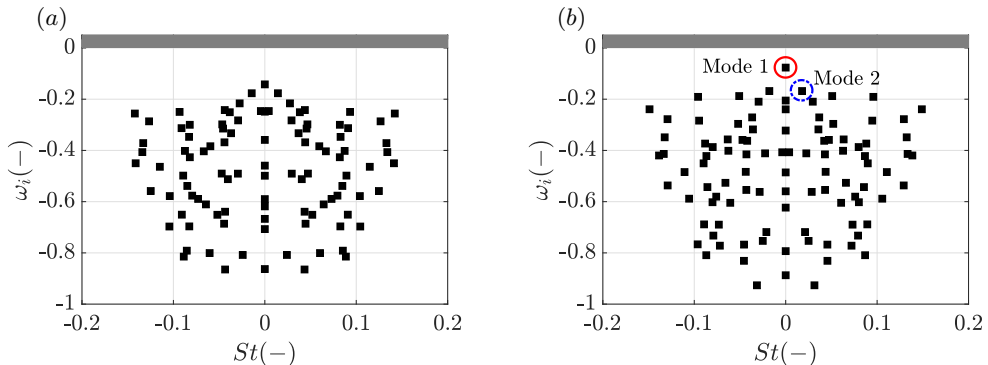


FIGURE 8. Global LSA spectrum for non-dimensional spanwise wavenumber $\beta = 0$ (a) and $\beta = 0.75$ (b). The eigenvalue is $\omega = \omega_i + \omega_r$, where ω_i is the growth rate and the Strouhal number is calculated based on ω_r . The least stable stationary (—) and travelling (- - -) mode are highlighted for $\beta = 0.75$.

Robinet (2007) and Toubert & Sandham (2009) in different types of separation bubbles. In particular, such a stationary global mode was related to a centrifugal instability mechanisms potentially leading to transition in LSBs by Rodríguez *et al.* (2013). The present analysis therefore suggests that a similar mechanism might be at play in TSBs. While the latter works revealed the presence of a global instability, the stable nature of the present modes matches well the results of Bugeat *et al.* (2022) and Sartor *et al.* (2015), in laminar and turbulent SBLIs, respectively.

As we progress from two-dimensional ($\beta = 0$) towards three-dimensional perturbations ($\beta = 0.75$), the least stable mode (Mode 1) moves closer to the stability threshold (figure 9). The growth rate ω_i of the least stable mode reaches its maximum for low non-zero β , after which it monotonically decreases for all $\beta > 0.75$. In relation to the bubble length L_b , this particular β corresponds to a wavelength λ_z approximately eight times the extent of the TSB ($\lambda_z \approx 8L_b$). This is in good agreement with the low- β region observed in the experiments summarized in section 2.2, where the low-frequency unsteadiness was shown to be characterized by a wavenumber of the order of $\beta \simeq 1$. Furthermore, the frequency of the least stable travelling mode (Mode 2) takes values between $St = 0.014 - 0.018$ in the low- β region ($\beta < 2$). This is also consistent with the low-frequency unsteadiness observed experimentally in the TSB.

Based on these results, it appears that both the first and second modes in the low- β region, although stable, would be reasonable candidates for the low-frequency unsteadiness if properly excited by external perturbations. To further differentiate between modes 1 and 2, we plot their streamwise component in figure 10. This particular choice of β coincides with the maximum observed in figure 9. We observe a least stable stationary mode (Mode 1) that is mainly located in the region surrounding and above the TSB (Fig. 10 (a)). This is consistent with the large-scale, “global” nature of the breathing motion, as depicted for example in the SPOD results of figure 2. While the corresponding travelling mode (Mode 2) shares qualitative similarities with Mode 1, we note that the observed structure is shifted towards the downstream part of the bubble and smaller in the wall-normal and streamwise directions (Fig. 10 (b)). Hence, based on its shape, relatively small decay rate at low spanwise wavenumber, and stationary character, Mode 1 thus appears to be a better candidate for the low-frequency unsteadiness. However, its stable character indicates that this mode is not capable of generating self-sustained oscillations

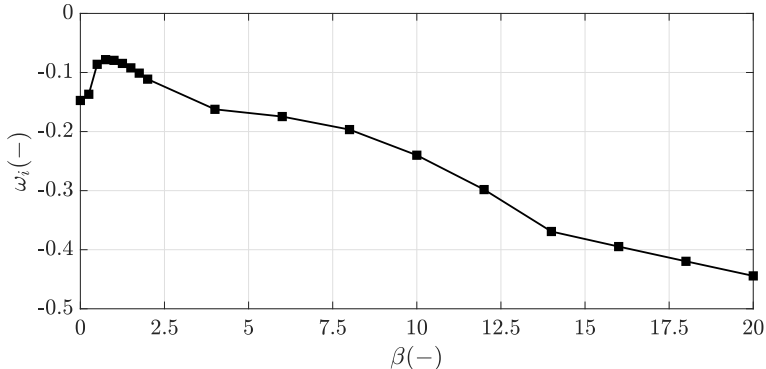


FIGURE 9. Growth rate ω_i from GLSA over non-dimensional spanwise wavenumber β . The least damped mode of the spectrum is depicted.

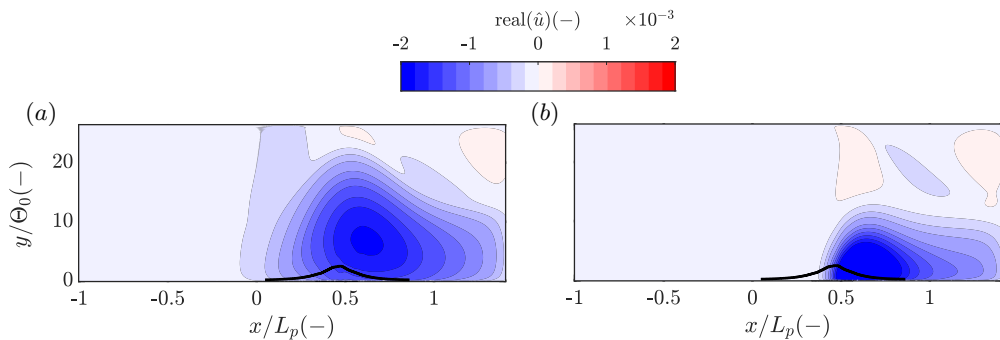


FIGURE 10. Streamwise component of GLSA Mode 1 (a) and Mode 2 (b) for non-dimensional spanwise wavenumber $\beta = 0.75$. The time-averaged location of the TSB is indicated by the dividing streamline $\bar{\Psi} = 0$ (—).

in the TSB. We now consider resolvent analysis to investigate the receptivity of this mode to external perturbations.

5.2. Resolvent analysis

In the previous section we established that the investigated TSB flow is globally stable in the asymptotic time limit. In order to study its response to forcing, we now proceed to outline results from the resolvent analysis, directing particular focus towards the low- β region as well as the low-frequency range. In figure 11 the optimal energy gain σ_1^2 of the RA is shown for different non-dimensional spanwise wavenumbers β . The Strouhal number is fixed at $St = 0.01$, corresponding to the characteristic low-frequency breathing motion. The optimal energy gain increases up to a maximum of $\beta = 2.75$, after which it monotonically decreases for $\beta > 2.75$. The peak amplitude is thus reached at a non-dimensional spanwise wavenumber that is slightly higher than for GLSA. The wavenumber $\beta = 2.75$ is also somewhat larger than the low- β region defined in section 2.2. However, in relation to the bubble length L_b , this particular β corresponds to a wavelength λ_z approximately twice the extent of the TSB ($\lambda_z \approx 2L_b$). We therefore conclude that the value $\beta = 2.75$ can still be considered low- β , as the associated wavelength is substantially larger than the TSB. In order to allow for a

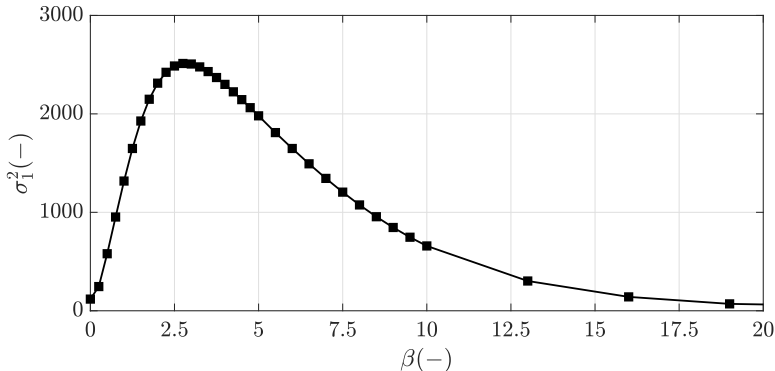


FIGURE 11. Optimal energy gain σ_1^2 from resolvent analysis for different non-dimensional spanwise wavenumbers β . The frequency is fixed at $St = 0.01$.

consistent comparison between GLSA and RA results, we will proceed to further analyze the non-dimensional spanwise wavenumbers $\beta = 0$ and $\beta = 0.75$.

We now investigate the behavior of the optimal energy gain σ_1^2 for different Strouhal numbers St , where we distinguish between the two-dimensional case ($\beta = 0$) and the three-dimensional case ($\beta = 0.75$). For $\beta = 0$, we obtain a distribution that monotonically increases up to a Strouhal number of $St \approx 0.1$, after which the optimal energy gain decreases again (Fig. 12 (a)). The associated (streamwise) optimal forcing and response are displayed in figure 13. At medium frequency ($St \approx 0.1$) and for two-dimensional perturbations ($\beta = 0$), the optimal forcing is located mostly upstream of the bubble. The resulting optimal response exhibits the typical alternating pattern of the Kelvin-Helmholtz (K-H) instability waves, which are tilted towards the direction of the base flow shear. For the present DNS base flow, it was shown in Cura *et al.* (2023) by means of local linear stability analysis, that the medium-frequency regime, characterized by the Strouhal number $St \approx 0.1$, is related to the roll-up and shedding of vortices through a shear layer instability. The present results confirm the latter analysis. Furthermore, the revealed structures strongly resemble the medium-frequency modes for the turbulent SWBLI from Sartor *et al.* (2015) and the laminar SWBLI from Bugeat *et al.* (2022). However, in the latter they were attributed to a convective instability reminiscent of the compressible counterpart of the Tollmien-Schlichting instability.

In the case of three-dimensional perturbations ($\beta = 0.75$), a substantial difference can be observed (Fig. 12 (b)). The highest energy gains are now obtained in the low-frequency range, after which a distribution similar to that of a low-pass filter becomes apparent. Here, a distinct drop in optimal gain σ_1^2 occurs in the range $St = 10^{-3} - 10^{-2}$, which is in good agreement with the Strouhal number $St \simeq 0.01$ reported in pre-multiplied PSDs describing the low-frequency unsteadiness (e.g., Fig. 4). We can further observe a small “hump” in the region of $St \approx 0.1$, which, yet again, can be associated with K-H instability. Interestingly, this medium-frequency hump is only observed in the narrow range of non-dimensional spanwise wavenumbers $0 < \beta < 1.25$. It is most pronounced for $\beta = 0.25$ and disappears for $\beta > 1$. The low-pass filter behavior on the other hand, can be observed for any low non-zero β .

We now define a decibel scale for the optimal gain σ_1

$$\sigma_{1,\text{dB}}(St) = 20 \log(\sigma_1(St)) \quad (5.1)$$

and apply the -3 dB rule to estimate the cut-off frequency of the filter function. This is

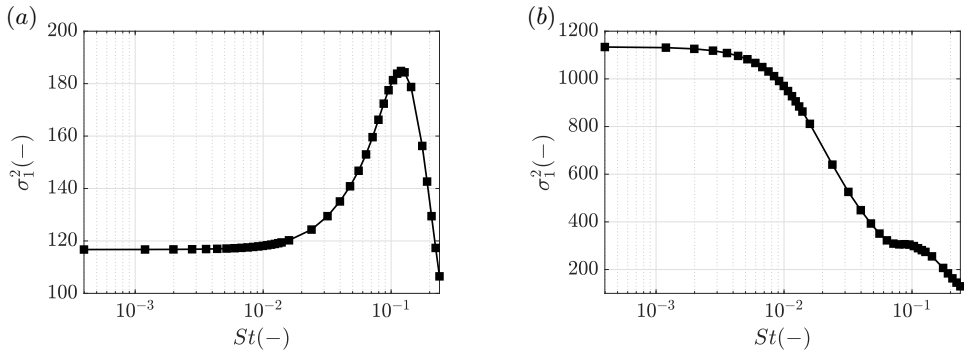


FIGURE 12. Optimal energy gain σ_1^2 from resolvent analysis versus different Strouhal numbers St for two-dimensional case $\beta = 0$ (a) and a sample three-dimensional case $\beta = 0.75$ (b).

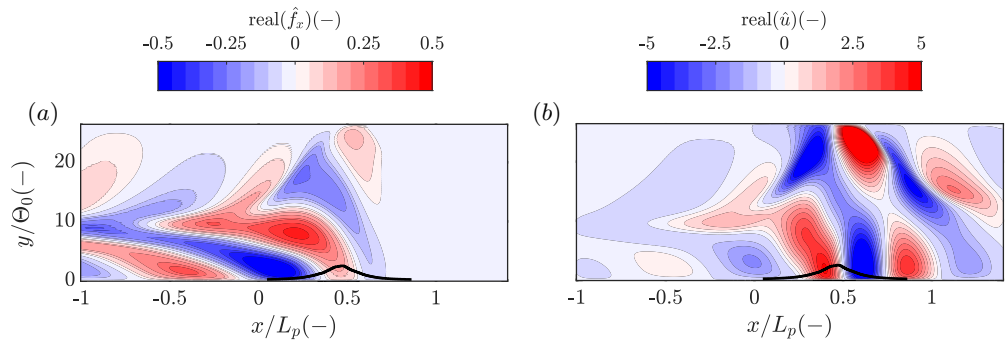


FIGURE 13. Streamwise component of optimal forcing \hat{f}_x (a) and response \hat{u} (b) for non-dimensional spanwise wavenumber $\beta = 0$ and $St = 0.12$. The time-averaged location of the TSB is indicated by the dividing streamline $\bar{\Psi} = 0$ (—).

shown in figure 14 (a), where the low-pass filter representation of σ_1 is shown for the non-dimensional spanwise wavenumber $\beta = 2$. We obtain a cut-off frequency corresponding to $St_c = 0.018$. Interestingly, the cut-off frequency monotonically increases from $\beta = 0.25$ to $\beta = 2$ and takes values between 0.006 and 0.018. Hence, all non-dimensional spanwise wavenumbers associated with the low non-zero- β regime reveal cut-off frequencies which are in good agreement with values reported for the low-frequency breathing phenomenon $St \simeq 0.01$ (e.g. Mohammed-Taifour & Weiss (2016); Le Floc'h *et al.* (2020); Steinfurth *et al.* (2022); Richardson *et al.* (2023)). Furthermore, from figure 14 (a) it becomes apparent that the low-pass filter representation of σ_1 indicates a first-order behaviour. After the cut-off frequency St_c , the amplitude of $20\log(\sigma_1)$ decreases approximately at the rate -20dB/dec , as indicated by the red-dashed line in figure 14 (a). This behavior can be observed for any low non-zero β . Interestingly, this first-order-filter character of low-frequency unsteadiness has already been observed in the incompressible TSB of Mohammed-Taifour & Weiss (2021). It is also a recurrent observation in turbulent SBLIs (Plotkin 1975; Toubert & Sandham 2011; Poggie *et al.* 2015). Furthermore, a similar low-pass filter model has also been found in the resolvent analysis of a laminar SBLI by Bugeat *et al.* (2022). Combined with these existing results, our new findings suggest that the low-pass filter model of separation bubble unsteadiness may be valid in a broad range of Reynolds and Mach numbers. In pre-multiplied form, the frequency response of

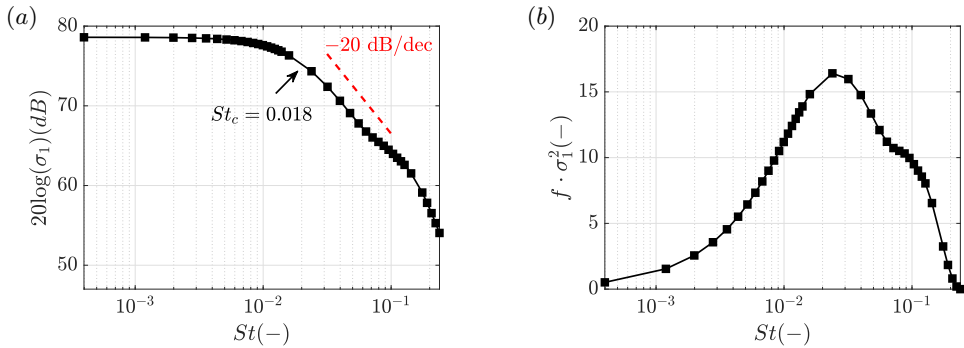


FIGURE 14. First-order low-pass filter representation of optimal gain from resolvent analysis $20\log(\sigma_1)$ (a) and pre-multiplied energy gain $f \cdot \sigma_1^2$ (b) versus different Strouhal numbers St (b). The non-dimensional spanwise wavenumber is $\beta = 2$. The Strouhal number St_c corresponding to the cut-off frequency based on the -3 dB rule is indicated in the figure. We further depict the characteristic slope of a first-order low-pass filter -20 dB/dec (---).

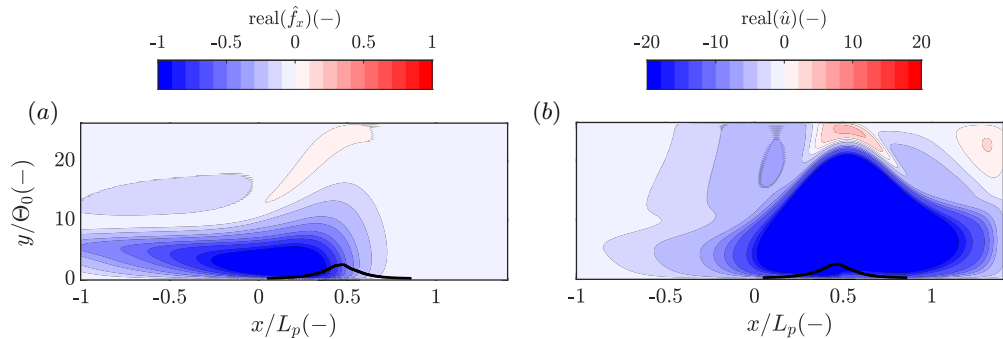


FIGURE 15. Streamwise component of optimal forcing \hat{f}_x (a) and response \hat{u} (b) for non-dimensional spanwise wavenumber $\beta = 0.75$ and $St = 0.01$. The time-averaged location of the TSB is indicated by the dividing streamline $\bar{\Psi} = 0$ (—).

first-order filters typically shows a maximum at a frequency close to the -3 dB cut off (Poggie *et al.* 2015). As can be observed in figure 14 (b), such a hump can also be observed for the energy gain $f \cdot \sigma_1^2$. The resulting curve is also similar to the pre-multiplied PSD of the wall pressure fluctuations shown in figure 4 (b).

In figure 15 the (streamwise) optimal forcing and response associated with the low-frequency, low non-zero- β regime are displayed. This is exemplary shown for $\beta = 0.75$ and $St = 0.01$. The optimal forcing is located mostly upstream of the bubble, encompassing a large portion of the domain. A large elongated structure can be observed, where the maximum amplitude is reached near the time-averaged separation point (Fig. 15 (a)). The resulting optimal response bounds the recirculation region and follows its shape (Fig. 15 (b)). Similar to the low-pass filter behavior of the optimal energy gain (Fig. 12), any non-dimensional spanwise wavenumber in the low non-zero- β regime exhibits similar low-frequency characteristics. That is, similar contours of optimal forcing and response could be observed for any (St, β) within this region. This behavior suggests that the receptivity at low-frequency is not driven by a unique frequency and spanwise wavenumber, but rather by a range of low Strouhal numbers ($St \simeq 0.01$) and low non-zero spanwise wavenumbers. Crucially, the shape and position of the optimal response closely

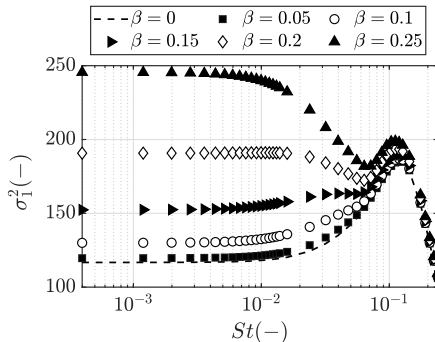


FIGURE 16. Optimal energy gain σ_1^2 from resolvent analysis versus different Strouhal numbers St for small spanwise wavenumbers $\beta \leq 0.25$. The represented optimal energy gains correspond to $\beta = 0$ (---), $\beta = 0.05$ (\blacksquare), $\beta = 0.1$ (\circ), $\beta = 0.15$ (\blacktriangleright), $\beta = 0.2$ (\diamond) and $\beta = 0.25$ (\blacktriangle).

resemble the least stable mode (Mode 1) of the GLSA. Therefore, our results suggest that the low-frequency unsteadiness in our TSB is driven by a modal mechanism, where the least stable global mode is selectively amplified for a range of (St, β) . In turn, since this global mode may be associated with a stable centrifugal mechanism, the results suggest that the TSB low-frequency unsteadiness is related to the excitation of such centrifugal dynamics by turbulence. This hypothesis will be further discussed in section 6.

5.2.1. Low non-zero- β region

So far, we have used the term “low non-zero spanwise wavenumber” loosely, assuming that certain properties of the optimal gain as well as their associated forcing and response can be recovered as long as $\beta \neq 0$ and $\lambda_z \gg L_b$. However, the transition from what we observe for two-dimensional perturbations ($\beta = 0$) to the behavior of what we dubbed the low non-zero- β region is not discrete, but rather continuous. Hence, for the sake of clarity and completeness, in this section, we take a closer look at the region $\beta \leq 0.25$. In figure 16 we plot the optimal energy gain σ_1^2 over different Strouhal numbers St for six spanwise wavenumbers $\beta \in [0, 0.25]$. For $\beta = 0$, we obtain the same distribution as shown in figure 12 (a). The distinct peak at $St \simeq 0.1$, which we previously associated with the K-H instability, remains visible for all β shown in figure 16. However, as β increases, the optimal energy gain σ_1^2 in the low-frequency region increases as well. Finally, for $\beta = 0.25$ we first observe the expected low-pass filter behavior, with dominant optimal energy gains in the low-frequency region. The associated contours of optimal forcing and response now appear similar to figure 15 (not shown here). This behavior can be observed up to approximately $\beta = 3$, after which the qualitative shape of optimal forcing and response starts to differ. Taking this into account, we may now adopt the (loose) definition of $\beta \in [0.25, 3]$ whenever we refer to the low non-zero- β region.

5.2.2. Three-dimensional structures

In the following, we investigate the three-dimensional structure of the resolvent modes in the low non-zero- β , low-frequency regime. For this purpose, we plot iso-surfaces of the streamwise (Fig. 17 (a, b)) and spanwise (Fig. 17 (c, d)) component of the optimal forcing and response. Iso-surfaces of $\pm 35\%$ of the forcings $|\hat{f}_x|, |\hat{f}_z|$ and the responses $|\hat{u}|, |\hat{w}|$ are displayed, respectively. The time-averaged location of the separation bubble is indicated by the grey-shaded region, which corresponds to the dividing streamline ($\bar{\Psi} = 0$). The frequency is fixed at $St = 0.01$ and the non-dimensional spanwise wavenumber is $\beta = 0.75$. In this representation, the distinction between optimal forcing and response is even

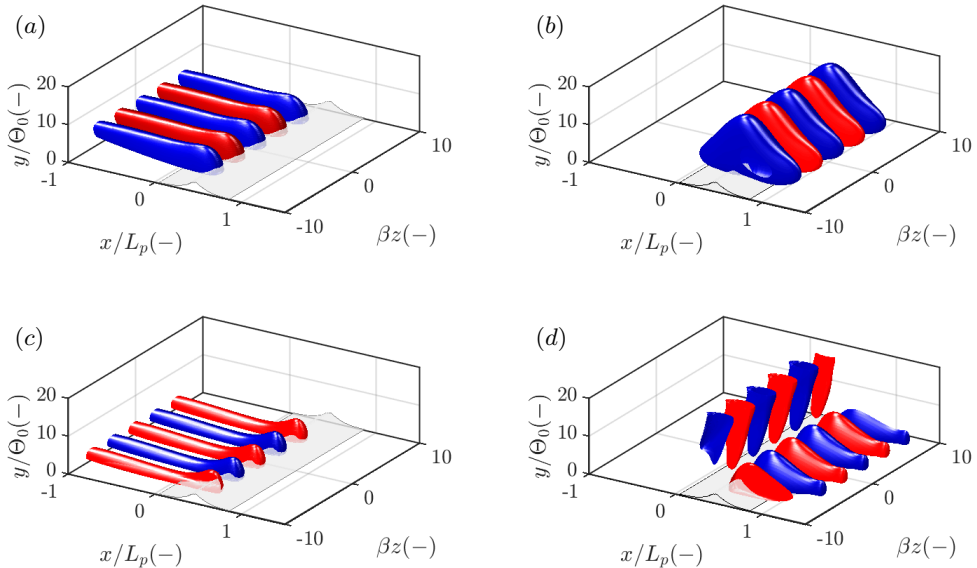


FIGURE 17. Streamwise component of optimal forcing \hat{f}_x (a) and response \hat{u} (b) and spanwise component of optimal forcing \hat{f}_z (c) and response \hat{w} (d) from RA for non-dimensional spanwise wavenumber $\beta = 0.75$. The real part of the modes is depicted. Iso-surfaces of $\pm 35\%$ of $\max|\hat{f}_x|$, $\max|\hat{u}|$ and $\max|\hat{f}_z|$, $\max|\hat{w}|$ are shown, respectively.

more prominent. While the optimal forcing is located mostly upstream and in the first half of the TSB (Figs. 17 (a, c)), the optimal responses \hat{u} , \hat{w} are located in the region surrounding the separation bubble. This particular spatial configuration of forcing and response suggests that upstream disturbances are a required contribution to the low-frequency unsteadiness. Notably, the elongated structures in the upstream region closely resemble boundary layer streaks, albeit with much larger spanwise wavelength compared to usual superstructures in turbulent boundary layers, as discussed in section 2. Whereas the streamwise component of forcing is concentrated to areas parallel to the bottom wall (Fig. 17 (a)), the structure of the spanwise component is slightly tilted upward in the TSB region in figure 17 (c). This behavior was also observed for the spanwise forcing at low β in Bugeat *et al.* (2022), even though the investigated flow was a laminar SBLI.

5.2.3. Sub-optimal energy gains

In this section, the behavior of the sub-optimal resolvent modes associated with $\sigma_2, \sigma_3, \dots, \sigma_n$ and their corresponding forcing fields is studied. Figure 18 shows the sub-optimal energy gains σ_n^2 at the fixed frequency $St = 0.01$ and for different non-dimensional spanwise wavenumbers β . Similar trends as for the optimal energy gain σ_1^2 can be observed. The sub-optimal energy gains monotonically increase up to a maximum at low/moderate β , after which they start to decay. The maximum of the curves, however, is slightly shifted towards higher β as compared to figure 11. For instance, σ_2^2 attains its maximum value for $\beta = 4.5$, which no longer aligns well with the previously defined region of low non-zero β observed in the experiments. Furthermore, the low-pass filter behavior observed in the optimal energy gain σ_1^2 is not as pronounced for the sub-optimal energy gains. Their behavior over different Strouhal numbers is shown in figure 19 for the two-dimensional case ($\beta = 0$) and the three-dimensional case ($\beta = 0.75$). For three-

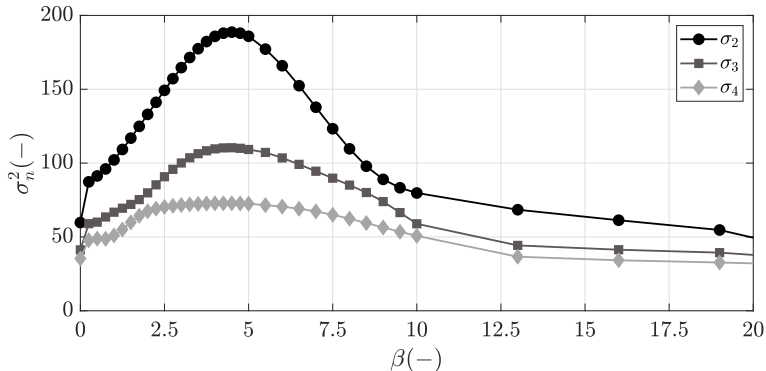


FIGURE 18. Sub-optimal energy gain σ_n^2 from resolvent analysis for different non-dimensional spanwise wavenumbers β . The frequency is fixed at $St = 0.01$. The displayed sub-optimal gains are σ_2 (\bullet), σ_3 (\blacksquare) and σ_4 (\blacklozenge).

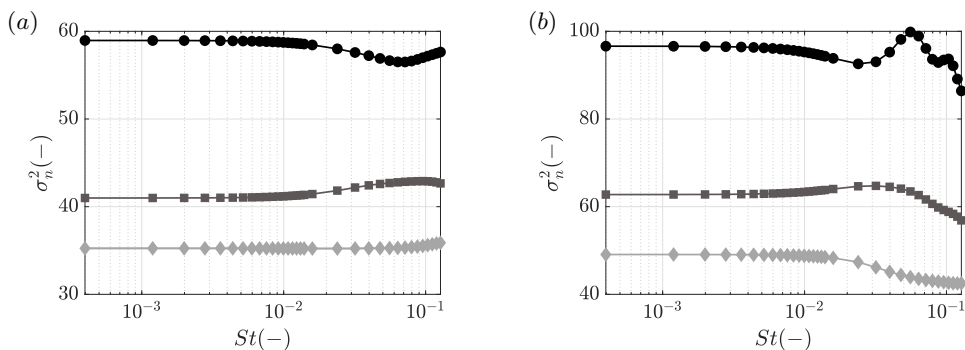


FIGURE 19. Sub-optimal energy gains σ_n^2 from resolvent analysis versus different Strouhal numbers St for two-dimensional case $\beta = 0$ (a) and a sample three-dimensional case $\beta = 0.75$ (b). The displayed sub-optimal energy gains are σ_2^2 (\bullet), σ_3^2 (\blacksquare) and σ_4^2 (\blacklozenge).

dimensional perturbations ($\beta = 0.75$) the sub-optimal energy gain σ_2^2 exhibits a very strong hump at $St = 0.06$ and a secondary hump at $St = 0.1$ (Fig. 19 (b)). The low-pass filter behavior is only visible for $St < 0.02$. Similar observations can be made for σ_3^2 . Here, the low-pass filter function is superimposed by a broadband hump centered around $St = 0.03$. Only the sub-optimal energy gain σ_4^2 displays the expected low-pass filter behavior with a reasonable cut-off frequency.

Generally speaking, the sub-optimal forcings and responses retain similar features as the optimal forcings and responses (figures 13, 15). However, additional structures away from the bubble and oriented along the base flow shear become apparent, see for example figure 20. Combined with the fact that the optimal gain is low rank, as indicated by $\sigma_1^2/\sigma_2^2 \approx 12$, this leads to the inference that the sub-optimal gains are less likely to be responsible for the receptivity at low frequency.

5.2.4. Effect of eddy viscosity

Up to this point, all presented results have been computed using the LNSE operator modelling part of the Reynolds stresses by means of an eddy-viscosity model. Here we briefly discuss the effects of neglecting the eddy viscosity ($\nu_t = 0$) on the forced dynamics of the bubble. In figure 21 the optimal energy gain σ_1^2 is displayed for the

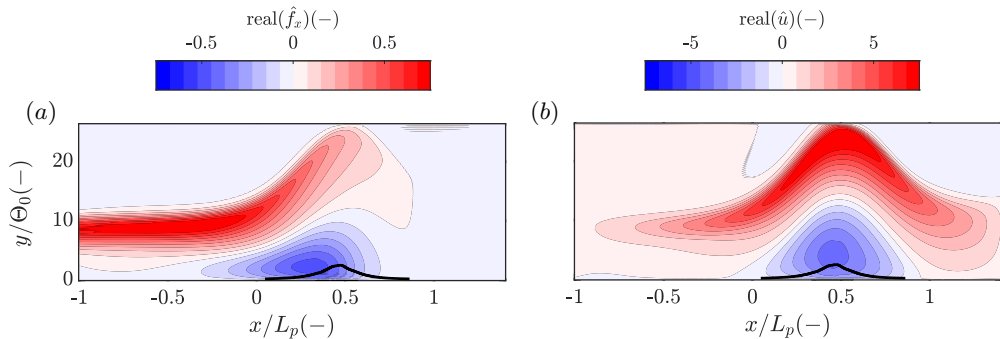


FIGURE 20. Streamwise component of sub-optimal forcing \hat{f}_x (a) and response \hat{u} (b) related to the sub-optimal energy gain σ_2^2 . The non-dimensional spanwise wavenumber and frequency are $\beta = 0.75$ and $St = 0.01$, respectively. The time-averaged location of the TSB is indicated by the dividing streamline $\bar{\Psi} = 0$ (—).

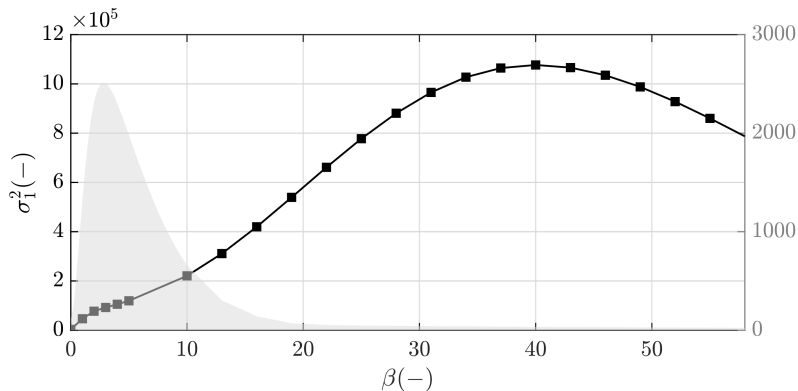


FIGURE 21. Optimal energy gain σ_1^2 from resolvent analysis when the terms related to the eddy-viscosity are neglected ($\nu_t = 0$) for different non-dimensional spanwise wavenumbers β (—■—). The frequency is fixed at $St = 0.01$. The optimal energy gain including the eddy-viscosity model in the LNSE operator is indicated as a grey-shaded region.

fixed frequency $St = 0.01$ and over different non-dimensional spanwise wavenumbers β . A strongly modified curve can be observed as compared to figure 11, where $\nu_t \neq 0$ (grey-shaded region). The distinct peak observed for $\beta = 2.75$ is now barely visible. Only a very slight “plateau” in the expected region of spanwise wavenumbers remains. On the other hand, a maximum for high non-dimensional spanwise wavenumbers becomes apparent at $\beta = 40$ ($\lambda_z \approx 0.15L_b$). This curve looks very similar to the distribution recovered in Bugeat *et al.* (2022) in a laminar SBLI, nevertheless, the local maximum at low non-zero β is less distinct in the present work. Remarkably, the modes at low non-zero β and low frequency $St \approx 0.01$ (not shown here) look very similar, regardless of whether or not a ν_t -model is employed.

6. Discussion

The results presented in section 5 using GLSA and RA indicate that the TSB base flow is globally stable but amplifies low-frequency ($St \simeq 0.01$) and low-wavenumber ($\beta \simeq 1$) upstream perturbations. In effect, the flow behaves as a selective amplifier and

the optimal energy gain computed from RA has the form of a first-order low-pass filter with a cut-off frequency of the order of $St \simeq 0.01$. In the present section we review these results and discuss them in light of the experimental database presented in section 2.

We commence by comparing the least stable mode from GLSA (Mode 1) to the optimal response from RA at the fixed frequency $St = 0.01$ and the non-dimensional spanwise wavenumber $\beta = 0.75$. Once again, it is crucial to mention that no distinct difference could be observed in the low-frequency, low non-zero- β regime in terms of the qualitative appearance of the RA modes. The streamwise (a, b), wall-normal (c, d), and spanwise component (e, f) of the respective modes are shown in figure 22. The GLSA mode is shown on the left (a, c, e) and the optimal response from RA is shown on the right (b, d, f). The optimal response is normalized by the optimal gain σ_1 to ensure comparability. It is apparent that all components $\hat{u}, \hat{v}, \hat{w}$ share strong similarities, with a comparable streamwise and wall-normal extent of the structures, a similar streamwise position x/L_p , and a matching phase. In the case of the streamwise modes \hat{u} this equates to a large-scale structure bounding the recirculation region and following its shape, as described in the previous sections. Moreover, the amplitudes of the modes are in good agreement and the maximum is reached in a similar region of x/L_p . Similar trends can be observed for the wall-normal and spanwise modes. Here, the structures are almost a perfect match in terms of position, phase and size. The obvious similarities between GLSA and RA modes strongly suggest that the receptivity at low frequency is most likely occurring from the excitation of the least stable global mode of the TSB (Mode 1).

We now proceed to investigate the low-frequency unsteadiness observed in the experimental data in more details. Specifically, our objective is to establish a connection between the low-frequency unsteadiness (breathing) and the described low-frequency receptivity. For this purpose, we first demonstrate that the observed low-frequency dynamics in the experimental data capture a large portion of the total turbulent kinetic energy (TKE) of the flow, that is, that the SPOD eigenvalues are of ‘‘low rank’’ in the low-frequency regime. Then, we proceed to show analogies between RA and SPOD results.

In figure 23 (a) the SPOD eigenvalues λ are depicted for all modes and all Strouhal numbers St . The eigenvalues are represented as the percentage of the total turbulent kinetic energy (TKE) density, ensuring that the summation of all eigenvalues equals 100%. From figure 23 it becomes apparent that the first mode is low-rank in the low-frequency region, particularly for $St \simeq 0.01$. Therefore, if we investigate the first SPOD mode λ_1 at the fixed frequency $St = 0.01$ (figure 23 (b)), we expect to capture a dominant feature of the flow. Here, the percentage of the TKE of the first mode is approximately 72%. Further evidence of the low-rank behavior of both the RA and SPOD modes is provided in figure 24. Here, we plot the ratio between the energy gains σ_1^2/σ_2^2 and between the SPOD eigenvalues λ_1/λ_2 . In both cases, in the low-frequency range, the low-rank behavior is of the order of 10.

The comparison between the highest ranking SPOD mode (a, c) and the optimal response of RA (b, d) is shown in figure 25 for $St = 0.01$ and $\beta = 0.25$. Here, only the x/L_p -region of the PIV measurement plane is depicted. Furthermore, we display the streamwise \hat{u} (a, b) and wall-normal \hat{v} (c, d) components, as only those are available from the experiment. In order to address the inherent arbitrariness of the phase in both SPOD and RA, the modes are subjected to a normalization. For this purpose, the phase of \hat{v} is set to zero, while $|\hat{v}| = 1$ at the fixed position $x/L_p = 0.2$ and $y/\theta_0 = 17$. From figure 25 it becomes apparent that the first SPOD mode and the optimal gain of RA are in close agreement when $St = 0.01$ and $\beta = 0.25$. The streamwise component \hat{u} displays a portion of the large structure surrounding the separation bubble as, e.g., previously

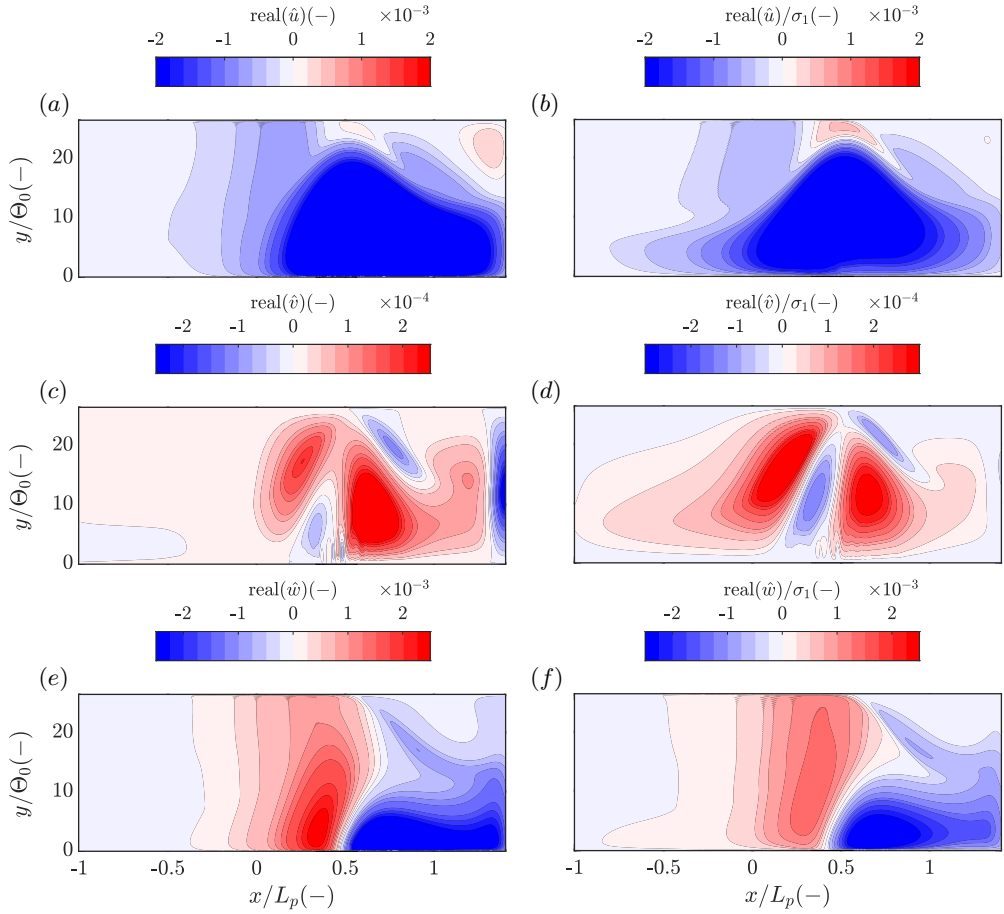


FIGURE 22. Global LSA mode 1 (*a, c, e*) and optimal response from RA (*b, d, f*) for non-dimensional spanwise wavenumber $\beta = 0.75$. The streamwise (*a, b*), wall-normal (*c, d*) and spanwise (*e, f*) modes are depicted, respectively.

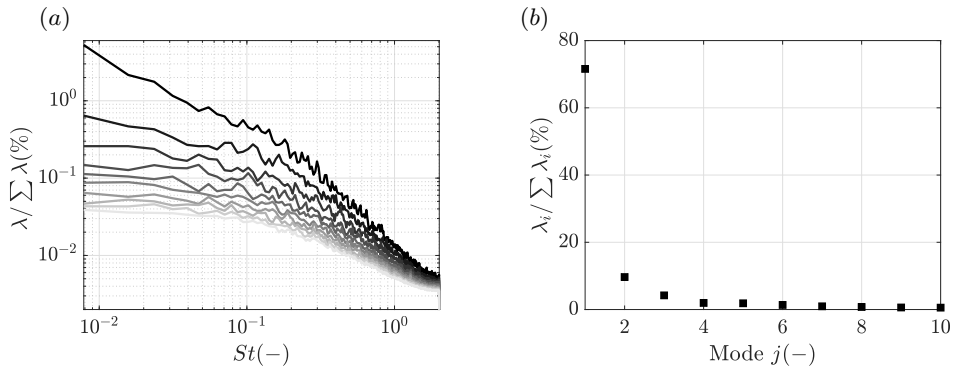


FIGURE 23. Spectral POD eigenvalues λ represented as the percentage of all modes (*a*) and SPOD eigenvalues λ_i at Strouhal number $St = 0.01$ represented as percentage of modes at low frequency (*b*). The modes 1 – 10 are depicted, respectively.

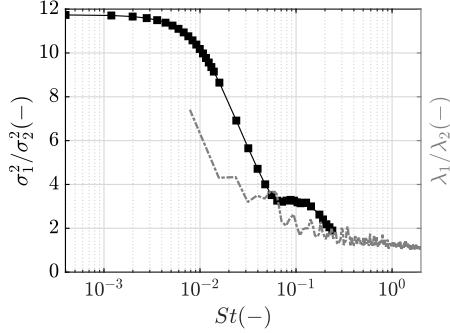


FIGURE 24. Low-rank behavior of energy gains σ_1^2/σ_2^2 of resolvent analysis (—■—) and SPOD eigenvalues λ_1/λ_2 (---) over different Strouhal numbers.

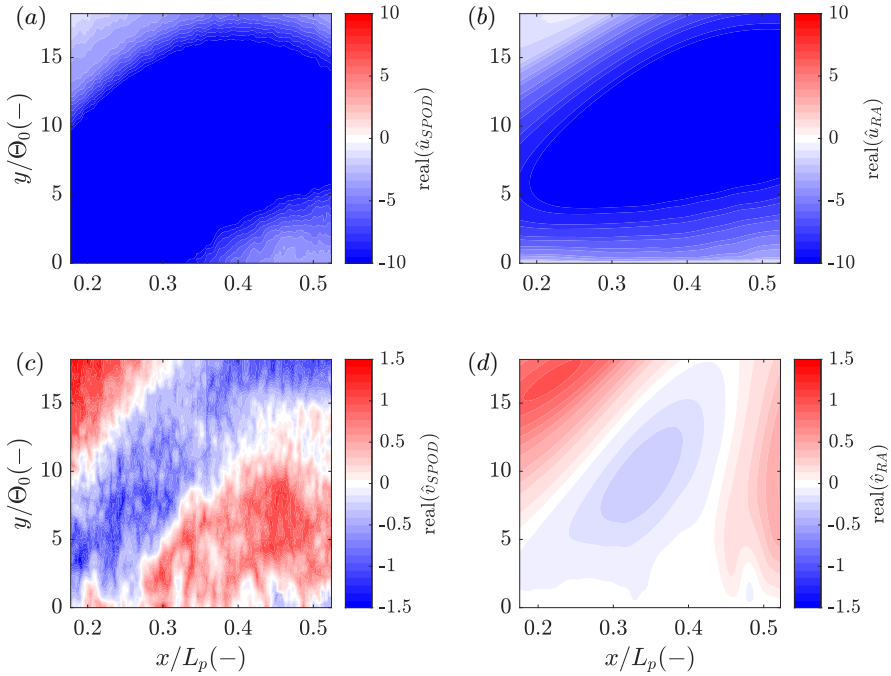


FIGURE 25. Comparison between leading SPOD mode of the fluctuating velocity field from experiments (a, c) and optimal response of RA (b, d) in the region of the PIV measurements. Results at low frequency $St = 0.01$ and with the highest alignment $\varphi = 0.95$, $\beta = 0.25$ are depicted. The streamwise (a, b) and wall-normal (c, d) component are displayed, respectively. All modes are scaled such that the wall-normal component is $|\hat{v}| = 1$ and the phase is zero at a fixed position in space ($x/L_p = 0.2, y/\Theta_0 = 16$).

shown in figure 15. The structures are tilted away from the solid bottom wall and follow the shape of the separated region. Furthermore, an excellent agreement between SPOD and RA can be observed in terms of amplitude and phase. The wall-normal component is also in good agreement with respect to the phase of the structures. A phase shift oriented approximately perpendicular to the shear layer can be observed. The amplitude, however, is slightly larger in the case of the first SPOD mode. The alignment φ , as introduced

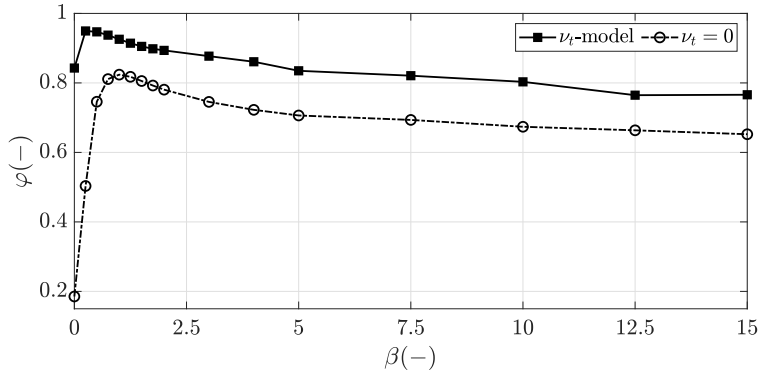


FIGURE 26. Alignment φ for different non-dimensional spanwise wavenumbers β . Results with (—■—) and without (---○---) an eddy-viscosity model are shown.

in section 4, is $\varphi = 0.95$. This large value of φ strongly suggests that the low-frequency breathing observed in the experiment is associated with the calculated RA response.

We have previously established that any RA mode with low non-zero β exhibits the same low-frequency characteristics when $St \approx 0.01$. In figure 26 we display the alignment φ between SPOD and RA over the non-dimensional spanwise wavenumber β at the fixed frequency $St = 0.01$. Both the analysis including an eddy-viscosity model and the analysis where $\nu_t = 0$, are depicted. We obtain two distributions of comparable qualitative nature. However, a strong offset between the alignment for the analysis including an eddy-viscosity model and the analysis where $\nu_t = 0$ is evident. Clearly, including a ν_t -model into the LNSE operator strongly increases the alignment with the experiment, as represented by the SPOD modes. This is particularly relevant since the overall shape of the modes is the same whether or not a ν_t -model is included. Interestingly, the significance of implementing an eddy-viscosity model to enhance the alignment between SPOD and RA has been demonstrated in prior studies. For example, Morra *et al.* (2019) presented evidence of its relevance in turbulent wall-bounded flows, while Pickering *et al.* (2020) extended this insight to a turbulent jet configuration.

In summary, the results presented so far demonstrate a strong alignment between the SPOD of the streamwise/wall normal velocity fluctuations obtained experimentally at low frequency and the optimal RA response computed in the low non-zero- β region. We further note that both the near wall velocity and wall-pressure fluctuations in the experiments indicate a characteristic wavenumber of the order of $\beta \simeq 1$ for the low-frequency breathing motion (e.g., figure 5). This cements the argument that the unsteadiness observed in the experiment is well described by the RA results. Hence, our conclusion is that the low-frequency breathing motion likely emanates from the excitation of the most weakly damped global mode in the TSB. This phenomenon is not dictated by a singular frequency but rather encompasses a range of low frequencies and low, non-zero spanwise wavenumbers. In effect, the TSB acts like a first-order low pass filter for upstream disturbances in the incoming turbulent boundary layer.

Interestingly, a low-pass filter model of low-frequency unsteadiness for separation bubbles has already been suggested in different flow configurations. Mohammed-Taifour & Weiss (2021), in a configuration similar to the present one, used upstream forcing to investigate the response of their TSB to upstream perturbations. They noted that the transient response of the separation line was compatible with a first-order low-pass filter model and observed consistent low-frequency dynamics in the unforced flow. For

the case of turbulent SBLIs, Poggie *et al.* (2015) investigated the frequency spectra of wall-pressure fluctuations in a variety of test cases and showed that despite differences in Reynolds and Mach numbers, the first-order model originally proposed by Plotkin (1975) and refined by Toubert & Sandham (2011) for shock-induced separation reasonably collapsed the results. Recently, Bugeat *et al.* (2022) proposed a similar low-pass-filter model for a laminar SBLI and demonstrated that this behaviour proceeds “from the excitation of a single, stable, steady global mode whose damping rate sets the time scale of the filter”. Hence, in the case of our TSB, the low-pass filter model is a direct consequence of our proposed mechanism of low-frequency unsteadiness since it is also based on the excitation of a stable global mode. Given the prevalence of low-pass filter behaviour in the literature on separation bubble unsteadiness, these results, combined with those of Bugeat *et al.* (2022) suggest that such a mechanism of low-frequency unsteadiness might occur in many types of separation bubbles.

Finally, we briefly come back to our original strategy of performing linear analysis on a DNS base flow that is similar, but not exactly the same, as the experimental flow field that we consider. In our case, the cross-validation between experimental unsteady data and the DNS base flow was necessary since the DNS did not include any unsteady data at the proper frequency, and the experimental data was not sufficiently resolved spatially to enable a proper linear analysis. Nevertheless, the concordance between the GLSA/RA results and the experimental data turned out to be close. This suggests that the phenomenology discovered in this work is not very sensitive to the exact geometry of the flow. Furthermore, the fact that the DNS base flow is devoid of any experimental artefacts like inflow unsteadiness, roughness effects, or the presence of wind-tunnel side walls, confirms that the low-frequency breathing motion observed in several low-speed and many high-speed experiments is a relevant fluid-dynamical phenomenon that is unlikely to be caused by wind-tunnel effects.

7. Conclusion

The objective of the present work was to perform modal and non-modal stability analysis on an incompressible, pressure-gradient-induced TSB to investigate the origin of the low-frequency breathing motion commonly observed in experimental studies. Specifically, we performed global linear stability analysis (GLSA) and resolvent analysis (RA) on a base flow consisting of the average flow field computed via DNS by Coleman *et al.* (2018), and we compared the results with the unsteady experimental measurements obtained by Le Floc’h *et al.* (2018, 2020) in a similar flow field.

GLSA revealed that the investigated TSB is globally stable in the asymptotic time limit for all frequencies and wavenumbers, indicating that no self-sustained (intrinsic) instability of the flow is driving the low-frequency unsteadiness. Interestingly, a region of low non-zero β was detected, for which the growth rate ω_i was closer to the stability threshold. This region was found to agree very well with the range of spanwise wavenumbers extracted from the experimental database at low frequency.

At low-frequency and low non-zero spanwise wavenumber, RA further revealed an optimal response strongly resembling the unsteady velocity signature of the breathing motion, which typically manifests as a large-scale coherent structure that follows the shape of the bubble. Specifically, a comparison between the first SPOD mode of the streamwise and wall-normal velocity fluctuations measured experimentally showed strong alignment with the optimal RA response. This, combined with the stable GLSA modes, indicates that the TSB behaves as an amplifier flow in the low-frequency regime. Furthermore, the optimal gain computed by RA at low non-zero wavenumber was shown to have the

characteristic shape of a first-order, low-pass filter with a cut-off frequency consistent with the low-frequency unsteadiness observed experimentally.

Finally, comparison between the least stable GLSA mode and the optimal RA response showed strong similarities in the low frequency and low wavenumber regime, and this for all velocity components. This behavior is considered a strong indication that the low-frequency oscillation is primarily driven by the least stable global mode, thereby characterizing the phenomenon as a forced modal mechanism, associated here with a centrifugal mechanism typical of other separation bubbles (Theofilis *et al.* 2000; Rodríguez *et al.* 2013). Hence, the main conclusion of this study is that the low-frequency breathing of the TSB is most likely driven by the excitation of a weakly damped global mode by the turbulent fluctuations in the incoming boundary layer. This is consistent with the mechanism recently proposed by Porter & Poggie (2019) for the case of turbulent SBLI flows. Our results also bears strong resemblance to the analysis of Bugeat *et al.* (2022) in a laminar SBLI, thereby suggesting that forced dynamics might be a common feature of separation bubbles in a wide range of flow conditions.

Appendix A. Matrix Operators

In this section, the matrix operators employed in the global stability and resolvent analysis are described. We commence by revisiting the equation

$$-i\omega\mathbf{M}\hat{\mathbf{q}} = (\mathbf{A} + \mathbf{N})\hat{\mathbf{q}} + \mathbf{B}\hat{\mathbf{f}}. \quad (\text{A } 1)$$

The linearized Navier-Stokes equations can be recast into an operator of the form

$$\mathbf{A} = \begin{bmatrix} \xi + \frac{\partial\bar{u}}{\partial x} - \frac{1}{Re}\nabla^2 & \frac{\partial\bar{u}}{\partial y} & 0 & \frac{\partial}{\partial x} \\ \frac{\partial\bar{v}}{\partial x} & \xi + \frac{\partial\bar{v}}{\partial y} - \frac{1}{Re}\nabla^2 & 0 & \frac{\partial}{\partial y} \\ 0 & 0 & \xi - \frac{1}{Re}\nabla^2 & i\beta \\ \frac{\partial}{\partial x} & \frac{\partial}{\partial y} & i\beta & 0 \end{bmatrix}, \quad (\text{A } 2)$$

where only the molecular viscosity in the flow is considered. Here $\xi = (\bar{u}\frac{\partial}{\partial x} + \bar{v}\frac{\partial}{\partial y})$ and $\nabla^2 = (\frac{\partial^2}{\partial x^2} + \frac{\partial^2}{\partial y^2} - \beta^2)$ is the Laplacian.

When the turbulence of the flow is considered by means of an eddy-viscosity model, the additional terms read

$$\mathbf{N} = \begin{bmatrix} -\eta - \frac{\partial\nu_t}{\partial x}\frac{\partial}{\partial x} - \nu_t\nabla^2 & -\frac{\partial\nu_t}{\partial y}\frac{\partial}{\partial x} & 0 & 0 \\ -\frac{\partial\nu_t}{\partial x}\frac{\partial}{\partial y} & -\eta - \frac{\partial\nu_t}{\partial y}\frac{\partial}{\partial y} - \nu_t\nabla^2 & 0 & 0 \\ -i\beta\frac{\partial\nu_t}{\partial x} & -i\beta\frac{\partial\nu_t}{\partial y} & -\eta - \nu_t\nabla^2 & 0 \\ 0 & 0 & 0 & 0 \end{bmatrix}, \quad (\text{A } 3)$$

where $\eta = (\frac{\partial\nu_t}{\partial x}\frac{\partial}{\partial x} + \frac{\partial\nu_t}{\partial y}\frac{\partial}{\partial y})$. The operator \mathbf{M} acts like a mass-like matrix in order to recover the continuity equation

$$\mathbf{M} = \begin{bmatrix} \mathcal{I} & 0 & 0 & 0 \\ 0 & \mathcal{I} & 0 & 0 \\ 0 & 0 & \mathcal{I} & 0 \\ 0 & 0 & 0 & 0 \end{bmatrix}, \quad (\text{A } 4)$$

where \mathcal{I} is the identity matrix of respective size. In the resolvent form

$$\hat{\mathbf{q}} = \mathbf{C}(-i\omega\mathbf{M} - \mathbf{A}_{2D,z})^{-1}\mathbf{B}\hat{\mathbf{f}}, \quad (\text{A } 5)$$

we define the additional matrix operators \mathbf{B} and \mathbf{C}

$$\mathbf{B} = \begin{bmatrix} b(x) & 0 & 0 \\ 0 & b(x) & 0 \\ 0 & 0 & b(x) \\ 0 & 0 & 0 \end{bmatrix}, \quad \mathbf{C} = \begin{bmatrix} c(x) & 0 & 0 & 0 \\ 0 & c(x) & 0 & 0 \\ 0 & 0 & c(x) & 0 \end{bmatrix}. \quad (\text{A } 6)$$

The sparse diagonal matrices act as filters that enforce constraints on the forcing and response, respectively. Here, $b(x) = 1$ in the region $x \in [0.05L_x, 0.85L_x]$, whereas $b(x) = 0$ in the remainder of the domain. Similarly, we set $c(x) = 1$ when $x \in [0.33L_x, 0.74L_x]$ and $c(x) = 0$ elsewhere. L_x is the length of the domain. The region $x \in [0.33L_x, 0.74L_x]$ is chosen as to agree with the PIV measurement region, which only covers a portion of the domain of the numerical data.

Appendix B. Boundary Conditions and Fringe Zone

The non-dimensional DNS base flow from Coleman *et al.* (2018), using the length scale $l^* = L_b$ and the time scale $t^* = L_b/u_\infty$, is depicted in Fig. 27. In the global stability and resolvent analysis, we subject the DNS base flow to periodic boundary conditions along the streamwise direction

$$u(x + L_\pi) = u(x), \quad (\text{B } 1)$$

$$v(x + L_\pi) = v(x), \quad (\text{B } 2)$$

where the periodicity length L_π is chosen according to $L_\pi = 0.9N_x$ and N_x is the streamwise dimension of the velocity fields. We further enforce that the disturbances decay at the solid top (∞) and bottom wall (0) according to

$$\hat{u}(0) = \hat{v}(0) = \hat{w}(0) = 0, \quad (\text{B } 3)$$

$$\hat{u}(\infty) = \hat{v}(\infty) = \hat{w}(\infty) = 0. \quad (\text{B } 4)$$

In order to suppress all disturbances $\hat{u}, \hat{v}, \hat{w}$ as well as forcings $\hat{f}_x, \hat{f}_y, \hat{f}_z$ in the region where the periodic boundary conditions are enforced, a fringe

$$\mathbf{S} = \begin{bmatrix} \sigma_f & 0 & 0 & 0 \\ 0 & \sigma_f & 0 & 0 \\ 0 & 0 & \sigma_f & 0 \\ 0 & 0 & 0 & 0 \end{bmatrix}, \quad (\text{B } 5)$$

is added to the two-dimensional LNSE operator $\mathbf{A}_{2D,z} = \mathbf{A} + \mathbf{N} + \mathbf{S}$. Here, σ_f is a sparse diagonal matrix with $\sigma_f = s_{\max} \cdot \exp(-(x - x_c)^2/L_f^2)$, s_{\max} is the maximum amplitude of the fringe, x_c is the center of the fringe and L_f is the length. The position and length of the fringe are chosen as $x_c \approx 6L_b$ and $L_f \approx 3.5\%L_x$, where L_x is the length of the domain.

Appendix C. Grid and Fringe Convergence

The grid convergence study is presented in Fig. 28. We portray the first ten singular values of the resolvent analysis at $\beta = 0$. Two Strouhal numbers are displayed: a Strouhal number $St = 0.01$, representative of the characteristic low-frequency breathing motion (a), and a Strouhal number in the medium-frequency regime $St = 0.1$ (b). Four different streamwise (N_x) and wall-normal (N_y) resolutions are depicted. For a resolution of $N_x \times N_y$ equal to 1200 x 160 or higher, a convergence of the results can be observed. Further

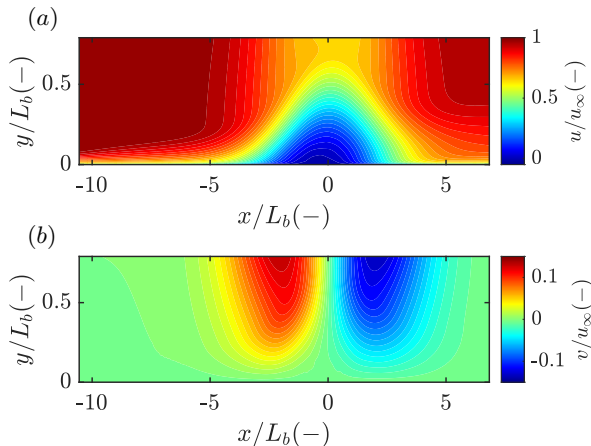


FIGURE 27. Non-dimensional DNS base flow using the length scale $l^* = L_b$ and the time scale $t^* = L_b/u_\infty$. The streamwise u/u_∞ (a) and wall-normal v/u_∞ (b) component of the time-averaged velocity field are displayed.

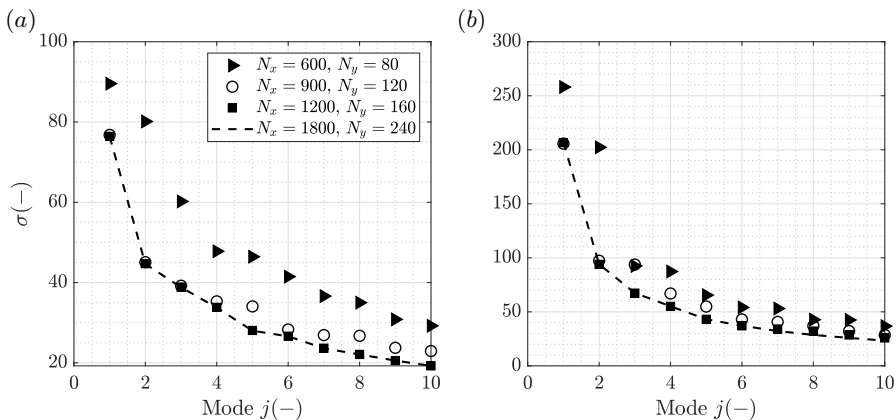


FIGURE 28. Grid convergence study for $St = 0.01$ (a) and $St = 0.1$ (b) based on Resolvent Analysis at $\beta = 0$. Grid independence of the singular values of the RA can be observed for $N_x \geq 1200$ and $N_y \geq 160$.

increasing the grid resolution yields no discernible influence on the singular values of the RA.

We illustrate the fringe convergence study in Fig. 29. Once again, we display $St = 0.01$ (a) and $St = 0.1$ (b). We maintain a fixed resolution $N_x = 1200$ and $N_y = 160$ for the analysis and test four different magnitudes s_{\max} . Fringe convergence can then be observed for magnitudes $s_{\max} \geq 2$.

In this work we perform the GLSA and RA analyses with a fringe magnitude of $s_{\max} = 5$. All resolvent analyses are performed with a resolution of $N_x = 1200$ and $N_y = 160$. A slightly higher resolution of $N_x = 1200$ and $N_y = 320$ is employed in the case of GLSA.

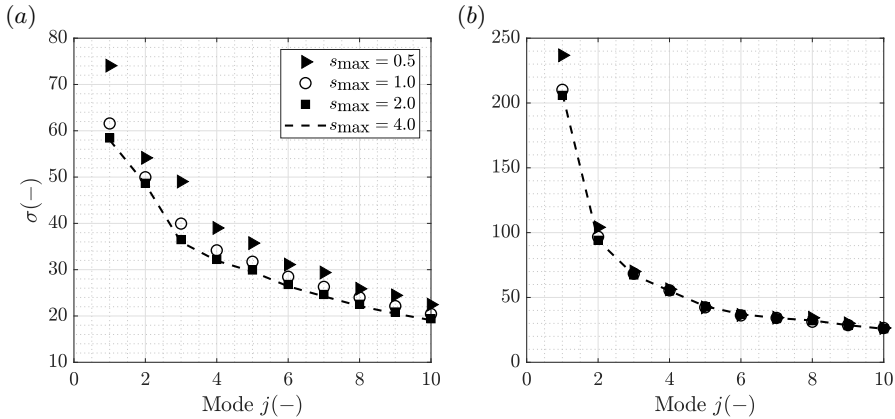


FIGURE 29. Fringe convergence study for $St = 0.01$ (a) and $St = 0.1$ (b) based on resolvent analysis at $\beta = 0$. Fringe independence of the singular values of the RA can be observed for $s_{\max} \geq 2$.

REFERENCES

- ABE, H. 2017 Reynolds-number dependence of wall-pressure fluctuations in a pressure-induced turbulent separation bubble. *Journal of Fluid Mechanics* **833**, 563–598.
- ABREU, L. I., CAVALIERI, A. V. G., SCHLATTER, P., VINUESA, R. & HENNINGSON, D. S. 2020 Spectral proper orthogonal decomposition and resolvent analysis of near-wall coherent structures in turbulent pipe flows. *Journal of Fluid Mechanics* **900**, A11.
- ABREU, L. I., TANARRO, A., CAVALIERI, A. V. G., SCHLATTER, P., VINUESA, R., HANIFI, A. & HENNINGSON, D. S. 2021 Spanwise-coherent hydrodynamic waves around flat plates and airfoils. *Journal of Fluid Mechanics* **927**, A1.
- ADLER, M. C. & GAITONDE, D. V. 2018 Dynamic linear response of a shock/turbulent-boundary-layer interaction using constrained perturbations. *Journal of Fluid Mechanics* **840**, 291–341.
- BARKLEY, D. 2006 Linear analysis of the cylinder wake mean flow. *Europhysics Letters* **75** (5), 750.
- BERESH, S. J., CLEMENS, N. T. & DOLLING, D. S. 2002 Relationship between upstream turbulent boundary-layer velocity fluctuations and separation shock unsteadiness. *AIAA journal* **40** (12), 2412–2422.
- BLANCO, D. C. P., MARTINI, E., SASAKI, K. & CAVALIERI, A. V. G. 2022 Improved convergence of the spectral proper orthogonal decomposition through time shifting. *Journal of Fluid Mechanics* **950**, A9.
- BOTTARO, A., CORBETT, P. & LUCHINI, P. 2003 The effect of base flow variation on flow stability. *Journal of Fluid Mechanics* **476**, 293–302.
- BOUTILIER, M. S. H. & YARUSEVYCH, S. 2013 Sensitivity of linear stability analysis of measured separated shear layers. *European Journal of Mechanics-B/Fluids* **37**, 129–142.
- BUGEAT, B., ROBINET, J.-CH., CHASSAING, J.-C. & SAGAUT, P. 2022 Low-frequency resolvent analysis of the laminar oblique shock wave/boundary layer interaction. *Journal of Fluid Mechanics* **942**, A43.
- CAVALIERI, A. V. G., JORDAN, P. & LESSHAFFT, L. 2019 Wave-packet models for jet dynamics and sound radiation. *Applied Mechanics Reviews* **71** (2), 020802.
- CHERRY, N. J., HILLIER, R. & LATOUR, M. E. M. P. 1984 Unsteady measurements in a separated and reattaching flow. *Journal of Fluid Mechanics* **144**, 13–46.
- CLEMENS, N. T. & NARAYANASWAMY, V. 2014 Low-frequency unsteadiness of shock wave/turbulent boundary layer interactions. *Annual Review of Fluid Mechanics* **46**, 469–492.
- COLEMAN, G. N. 2018 Dns: 2-d turbulent separation bubbles.
- COLEMAN, G. N., RUMSEY, C. L. & SPALART, P. R. 2018 Numerical study of turbulent

- separation bubbles with varying pressure gradient and reynolds number. *Journal of Fluid Mechanics* **847**, 28–70.
- CROW, S. C. & CHAMPAGNE, F. H. 1971 Orderly structure in jet turbulence. *Journal of fluid mechanics* **48** (3), 547–591.
- CURA, C., HANIFI, A. & WEISS, J. 2023 Medium-frequency unsteadiness in a turbulent separation bubble. In *AIAA SCITECH 2023 Forum*, p. 0095.
- DAU, K., BORGMANN, D., LITTLE, J. C. & WEISS, J. 2023 Investigation of low frequency unsteadiness in the turbulent separation bubble produced by a wall mounted hump. In *AIAA AVIATION 2023 Forum*, p. 4008.
- DEL ALAMO, J. C. & JIMENEZ, J. 2006 Linear energy amplification in turbulent channels. *Journal of Fluid Mechanics* **559**, 205–213.
- DOLLING, D. S. 2001 Fifty years of shock-wave/boundary-layer interaction research: what next? *AIAA journal* **39** (8), 1517–1531.
- DOVGAL, A. V., KOZLOV, V. V. & MICHALKE, A. 1994 Laminar boundary layer separation: instability and associated phenomena. *Progress in Aerospace Sciences* **30** (1), 61–94.
- DUSSAUGE, J.-P., DUPONT, P. & DEBIÈVE, J.-F. 2006 Unsteadiness in shock wave boundary layer interactions with separation. *Aerospace Science and Technology* **10** (2), 85–91.
- EATON, J. K. & JOHNSTON, J. P. 1981 A review of research on subsonic turbulent flow reattachment. *AIAA journal* **19** (9), 1093–1100.
- EHRENSTEIN, U. & GALLAIRE, F. 2008 Two-dimensional global low-frequency oscillations in a separating boundary-layer flow. *Journal of Fluid Mechanics* **614**, 315–327.
- GAITONDE, D. V. 2015 Progress in shock wave/boundary layer interactions. *Progress in Aerospace Sciences* **72**, 80–99.
- GANAPATHISUBRAMANI, B., CLEMENS, N. T. & DOLLING, D. S. 2007 Effects of upstream boundary layer on the unsteadiness of shock-induced separation. *Journal of fluid Mechanics* **585**, 369–394.
- GANAPATHISUBRAMANI, B., LONGMIRE, E. K. & MARUSIC, I. 2003 Characteristics of vortex packets in turbulent boundary layers. *Journal of Fluid Mechanics* **478**, 35–46.
- HUERRE, P. & MONKEWITZ, P. A. 1990 Local and global instabilities in spatially developing flows. *Annual review of fluid mechanics* **22** (1), 473–537.
- HUTCHINS, N. & MARUSIC, I. 2007 Evidence of very long meandering features in the logarithmic region of turbulent boundary layers. *Journal of Fluid Mechanics* **579**, 1–28.
- HWANG, Y. & COSSU, C. 2010 Linear non-normal energy amplification of harmonic and stochastic forcing in the turbulent channel flow. *Journal of Fluid Mechanics* **664**, 51–73.
- KIYA, M. & SASAKI, K. 1983 Structure of a turbulent separation bubble. *Journal of Fluid Mechanics* **137**, 83–113.
- LARCHEVÊQUE, L. 2020 Normalizing low-frequency unsteadiness in compressible separated flows (AIAA 2020-0561). In *AIAA SciTech 2020 Forum*.
- LE FLOCH, A., MOHAMMED-TAIFOUR, A., WEISS, J., DUFRESNE, L., VÉTEL, J. & JONDEAU, E. 2016 Effect of boundary-layer superstructures on separation bubble unsteadiness .
- LE FLOC'H, A., WEISS, J., MOHAMMED-TAIFOUR, A. & DUFRESNE, L. 2020 Measurements of pressure and velocity fluctuations in a family of turbulent separation bubbles. *Journal of Fluid Mechanics* **902**.
- LE FLOC'H, A. S., MOHAMMED-TAIFOUR, A. T., DUFRESNE, L. & WEISS, J. 2018 Spanwise aspects of unsteadiness in a pressure-induced turbulent separation bubble. In *2018 Fluid Dynamics Conference*, p. 3538.
- LESSHAFFT, L., SEMERARO, O., JAUNET, V., CAVALIERI, A. V. G. & JORDAN, P. 2019 Resolvent-based modeling of coherent wave packets in a turbulent jet. *Physical Review Fluids* **4** (6), 063901.
- LUMLEY, J. L. 1970 Stochastic tools in turbulence, volume 12 of. *Applied Mathematics and Mechanics, An International Series of Monographs* .
- MABEY, D. G. 1972 Analysis and correlation of data on pressure fluctuations in separated flow. *Journal of Aircraft* **9** (9), 642–645.
- MARQUET, O., SIPP, D., CHOMAZ, J.-M. & JACQUIN, L. 2008 Amplifier and resonator dynamics of a low-reynolds-number recirculation bubble in a global framework. *Journal of Fluid Mechanics* **605**, 429–443.

- McKEON, B. J. & SHARMA, A. S. 2010 A critical-layer framework for turbulent pipe flow. *Journal of Fluid Mechanics* **658**, 336–382.
- MICHALKE, A. 1984 Survey on jet instability theory. *Progress in Aerospace Sciences* **21**, 159–199.
- MOHAMMED-TAIFOUR, A. 2017 Instationnarités dans une bulle de décollement turbulente: étude expérimentale. PhD thesis, École de technologie supérieure.
- MOHAMMED-TAIFOUR, A., SCHWAAB, Q., PIOTON, J. & WEISS, J. 2015 A new wind tunnel for the study of pressure-induced separating and reattaching flows. *The Aeronautical Journal* **119** (1211), 91–108.
- MOHAMMED-TAIFOUR, A. & WEISS, J. 2016 Unsteadiness in a large turbulent separation bubble. *Journal of Fluid Mechanics* **799**, 383–412.
- MOHAMMED-TAIFOUR, A. & WEISS, J. 2021 Periodic forcing of a large turbulent separation bubble. *Journal of Fluid Mechanics* **915**, A24.
- MORRA, P., NOGUEIRA, P. A. S., CAVALIERI, A. V. G. & HENNINGSON, D. S. 2021 The colour of forcing statistics in resolvent analyses of turbulent channel flows. *Journal of Fluid Mechanics* **907**, A24.
- MORRA, P., SEMERARO, O., HENNINGSON, D. S. & COSSU, C. 2019 On the relevance of reynolds stresses in resolvent analyses of turbulent wall-bounded flows. *Journal of Fluid Mechanics* **867**, 969–984.
- NA, Y. & MOIN, P. 1998 Direct numerical simulation of a separated turbulent boundary layer. *Journal of Fluid Mechanics* **374**, 379–405.
- NISHIOKA, M., ASAI, M. & YOSHIDA, S. 1990 Control of flow separation by acoustic excitation. *AIAA journal* **28** (11), 1909–1915.
- NOGUEIRA, P. A. S., MORRA, P., MARTINI, E., CAVALIERI, A. V. G. & HENNINGSON, D. S. 2021 Forcing statistics in resolvent analysis: application in minimal turbulent couette flow. *Journal of Fluid Mechanics* **908**, A32.
- PICKERING, E., RIGAS, G., NOGUEIRA, P. A. S., CAVALIERI, A. V. G., SCHMIDT, O. T. & COLONIUS, T. 2020 Lift-up, kelvin–helmholtz and orr mechanisms in turbulent jets. *Journal of Fluid Mechanics* **896**, A2.
- PIPONIAU, S., DUSSAUGE, J.-P., DEBIEVE, J.-F. & DUPONT, P. 2009 A simple model for low-frequency unsteadiness in shock-induced separation. *Journal of Fluid Mechanics* **629**, 87–108.
- PIROZZOLI, S. & GRASSO, F. 2006 Direct numerical simulation of impinging shock wave/turbulent boundary layer interaction at $m=2.25$. *Physics of fluids* **18** (6).
- PLOTKIN, K. J. 1975 Shock wave oscillation driven by turbulent boundary-layer fluctuations. *AIAA Journal* **13** (8), 1036–1040.
- POGGIE, J., BISEK, N. J., KIMMEL, R. L. & STANFIELD, S. A. 2015 Spectral characteristics of separation shock unsteadiness. *AIAA Journal* **53** (1), 200–214.
- PORTER, K. M. & POGGIE, J. 2019 Selective upstream influence on the unsteadiness of a separated turbulent compression ramp flow. *Physics of Fluids* **31** (1).
- PRIEBE, S., TU, J. H., ROWLEY, C. W. & MARTÍN, M. P. 2016 Low-frequency dynamics in a shock-induced separated flow. *Journal of Fluid Mechanics* **807**, 441–477.
- RAJAEI, M., KARLSSON, S. K. F. & SIROVICH, L. 1994 Low-dimensional description of free-shear-flow coherent structures and their dynamical behaviour. *Journal of Fluid Mechanics* **258**, 1–29.
- REYNOLDS, W. C. & HUSSAIN, A. K. M. F. 1972 The mechanics of an organized wave in turbulent shear flow. part 3. theoretical models and comparisons with experiments. *Journal of Fluid Mechanics* **54** (2), 263–288.
- RICHARDSON, R., ZHANG, Y., CATTAFESTA, L. N. & WU, W. 2023 Low frequency characteristics of a pressure-gradient induced turbulent separation bubble. In *AIAA SCITECH 2023 Forum*, p. 0079.
- ROBINET, J.-CH. 2007 Bifurcations in shock-wave/laminar-boundary-layer interaction: global instability approach. *Journal of Fluid Mechanics* **579**, 85–112.
- RODRÍGUEZ, D. & GENNARO, E. M. 2017 Three-dimensional flow stability analysis based on the matrix-forming approach made affordable. In *Spectral and High Order Methods for Partial Differential Equations ICOSAHOM 2016: Selected Papers from the ICOSAHOM conference, June 27-July 1, 2016, Rio de Janeiro, Brazil*, pp. 639–650. Springer.

- RODRÍGUEZ, D., GENNARO, E. M. & JUNIPER, M. P. 2013 The two classes of primary modal instability in laminar separation bubbles. *Journal of Fluid Mechanics* **734**, R4.
- SANSICA, A., SANDHAM, N. D. & HU, Z. 2016 Instability and low-frequency unsteadiness in a shock-induced laminar separation bubble. *Journal of Fluid Mechanics* **798**, 5–26.
- SARTOR, F., METTOT, C., BUR, R. & SIPP, D. 2015 Unsteadiness in transonic shock-wave/boundary-layer interactions: experimental investigation and global stability analysis. *Journal of Fluid Mechanics* **781**, 550–577.
- SASAKI, K., BARROS, D. C., CAVALIERI, A. V. G. & LARCHEVÊQUE, L. 2021 Causality in the shock wave/turbulent boundary layer interaction. *Physical Review Fluids* **6** (6), 064609.
- SCHMIDT, O. T., TOWNE, A., COLONIUS, T., CAVALIERI, A. V. G., JORDAN, P. & BRÈS, G. A. 2017 Wavepackets and trapped acoustic modes in a turbulent jet: coherent structure eduction and global stability. *Journal of Fluid Mechanics* **825**, 1153–1181.
- SIPP, D. & LEBEDEV, A. 2007 Global stability of base and mean flows: a general approach and its applications to cylinder and open cavity flows. *Journal of Fluid Mechanics* **593**, 333–358.
- STEINFURTH, B., CURA, C. & WEISS, J. 2022 Three-dimensional effects associated with the low-frequency breathing motion of a turbulent separation bubble. In *20th International Symposium on Application of Laser and Imaging Techniques to Fluid Mechanics, Lisbon*.
- THEOFILIS, V. 2003 Advances in global linear instability analysis of nonparallel and three-dimensional flows. *Progress in aerospace sciences* **39** (4), 249–315.
- THEOFILIS, V. 2011 Global linear instability. *Annual Review of Fluid Mechanics* **43**, 319–352.
- THEOFILIS, V., HEIN, S. & DALLMANN, U. 2000 On the origins of unsteadiness and three-dimensionality in a laminar separation bubble. *Philosophical Transactions of the Royal Society of London. Series A: Mathematical, Physical and Engineering Sciences* **358** (1777), 3229–3246.
- TOMKINS, C. D. & ADRIAN, R. J. 2003 Spanwise structure and scale growth in turbulent boundary layers. *Journal of Fluid Mechanics* **490**, 37–74.
- TOUBER, E. & SANDHAM, N. 2011 Low-order stochastic modelling of low-frequency motions in reflected shock-wave/boundary-layer interactions. *Journal of Fluid Mechanics* **671**, 417–465.
- TOUBER, E. & SANDHAM, N. D. 2009 Large-eddy simulation of low-frequency unsteadiness in a turbulent shock-induced separation bubble. *Theoretical and computational fluid dynamics* **23**, 79–107.
- TOWNE, A., CAVALIERI, A. V. G., JORDAN, P., COLONIUS, T., SCHMIDT, O., JAUNET, V. & BRÈS, G. A. 2017 Acoustic resonance in the potential core of subsonic jets. *Journal of Fluid Mechanics* **825**, 1113–1152.
- TOWNE, A., SCHMIDT, O. T. & COLONIUS, T. 2018 Spectral proper orthogonal decomposition and its relationship to dynamic mode decomposition and resolvent analysis. *Journal of Fluid Mechanics* **847**, 821–867.
- WEISS, J., LITTLE, J., THREADGILL, J. & GROSS, A. 2021 Low-frequency unsteadiness in pressure-induced separation bubbles (AIAA 2021-1324). In *AIAA SciTech 2021 Forum*.
- WEISS, J., MOHAMMED-TAIFOUR, A. & SCHWAAB, Q. 2015 Unsteady behavior of a pressure-induced turbulent separation bubble. *AIAA Journal* **53** (9), 2634–2645.
- WEISS, J., STEINFURTH, B., CHAMARD, L., GIANI, A. & COMBETTE, P. 2022 Spectral proper orthogonal decomposition of unsteady wall shear stress under a turbulent separation bubble. *AIAA Journal* **60** (4), 2150–2159.
- WU, W., MENEVEAU, C. & MITTAL, R. 2020 Spatio-temporal dynamics of turbulent separation bubbles. *Journal of Fluid Mechanics* **883**.
- YARUSEVYCH, S., SULLIVAN, P. E. & KAWALL, J. G. 2006 Coherent structures in an airfoil boundary layer and wake at low reynolds numbers. *Physics of Fluids* **18** (4).
- ZARE, A., JOVANOVIĆ, M. R. & GEORGIU, T. T. 2017 Colour of turbulence. *Journal of Fluid Mechanics* **812**, 636–680.